PERGAMON

Progress in Materials Science 46 (2001) 505–553

Progress in Materials Science

www.elsevier.com/locate/pmatsci

Mechanisms controlling the durability of thermal barrier coatings

A.G. Evans [a,*], D.R. Mumm [a], J.W. Hutchinson [b], G.H. Meier [c], F.S. Pettit [c]

[a] *Materials Institute, Princeton University, Princeton, NJ 08540, USA*
[b] *Division of Engineering and Applied Sciences, Harvard University, Cambridge, MA 02138, USA*
[c] *Department of Materials Science and Engineering, University of Pittsburgh, Pittsburgh, PA 15261, USA*

Received 25 August 2000; accepted 10 October 2000

Abstract

The durability of thermal barrier coatings is governed by a sequence of crack nucleation, propagation and coalescence events that accumulate prior to final failure by large scale buckling and spalling. Because of differing manufacturing approaches and operating scenarios, several specific mechanisms are involved. These mechanisms have begun to be understood. This article reviews this understanding and presents relationships between the durability, the governing material properties and the salient morphological features. The failure is ultimately connected to the large residual compression in the thermally grown oxide through its roles in amplifying imperfections near the interface. This amplification induces an energy release rate at cracks emanating from the imperfections that eventually buckle and spall the TBC.

Contents

* Corresponding author. Tel.: +1-609-258-4762; fax: +1-609-258-1177.
E-mail address: anevans@princeton.edu (A.G. Evans).

0079-6425/01/$ - see front matter
PII: S0079-6425(00)00020-7

1. Background

1.1. The system

Thermal barrier coatings (TBCs) are widely used in turbines for propulsion and power generation [1–9]. They comprise thermally insulating materials having sufficient thickness and durability that they can sustain an appreciable temperature difference between the load bearing alloy and the coating surface. The benefit of these coatings results from their ability to sustain high thermal gradients in the presence of adequate back-side cooling. Lowering the temperature of the metal substrate prolongs the life of the component: whether from environmental attack, creep rupture, or fatigue. In addition, by reducing the thermal gradients in the metal, the coating diminishes the driving force for thermal fatigue. Both of these benefits can be traded off in design for greater component durability, or for reduced cooling air or for higher gas temperature/improved system efficiency. As a result, TBCs have been increasingly used in turbine engines. Successful implementation has required comprehensive testing protocols, facilitated by engineering models [9–12]. Expanded application to more demanding scenarios (Fig. 1) requires that their basic thermo-mechanical characteristics be understood and quantified. This need provides the opportunities and challenges discussed in this article.

There are *four primary constituents* in a thermal protection system (Fig. 2). They comprise (i) the TBC itself, (ii) the superalloy substrate, (iii) an aluminum containing bond coat (BC) between the substrate and the TBC, and (iv) a thermally grown oxide (TGO), predominantly alumina, that forms between the TBC and the BC. The TBC is the insulator, the TGO on the BC provides the oxidation protection and the alloy sustains the structural loads. The TGO is a reaction product. Each of these elements is dynamic and all interact to control the performance and durability.

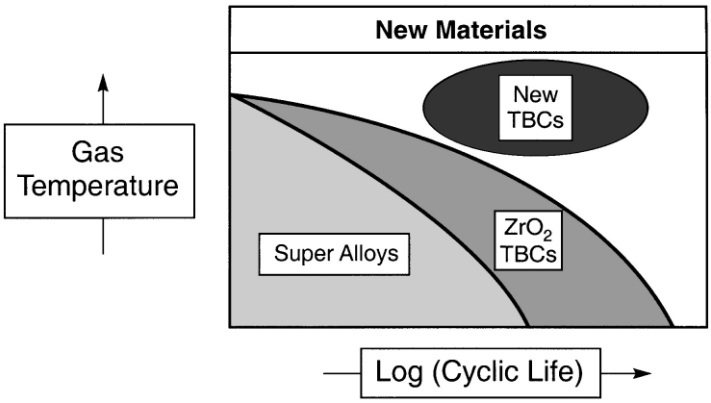

Fig. 1. Schematic indicating the operating domain for TBCs and the challenge for a new generation of materials.

The thermal barrier coating is a thermally insulating, "strain tolerant" oxide. Zirconia has emerged as the preferred material, stabilized into its cubic/tetragonal forms by the addition of yttria in solid solution. This material has low thermal conductivity ($\sim$1 W/m^2 K) with minimal temperature sensitivity (Fig. 3) [13,83]. The thermal resistance at lower temperatures corresponds to a phonon mean free path governed by structural vacancy scattering. Complex oxides having even lower conduction are being investigated, but there is no affirmation of their viability as TBCs. Strain tolerance is designed into the material to avoid instantaneous delamination from the thermal expansion misfit. Two methods are used to deposit strain-tolerant TBCs. Electron beam physical vapor deposition (EB-PVD) evaporates the oxide from an ingot and directs the vapor onto the preheated component [2,5,14]. The deposition conditions are designed to create a columnar grain structure with multiscale porosity (Fig. 2) that provides the strain tolerance and also reduces the thermal conductivity (to about 0.5 W/m K, Fig. 3). Air plasma spray (APS) deposition is a lower cost alternative [15–17]. The deposition is designed to incorporate intersplat porosity and a network of crack-like voids that again provides some strain tolerance, while lowering the thermal conductivity.

The thermally grown oxide has a major influence on TBC durability [8–12,18–20]. The bond coat alloy is designed as a local Al reservoir (Fig. 2), enabling α-alumina to form in preference to other oxides, as oxygen ingresses through the TBC (which is

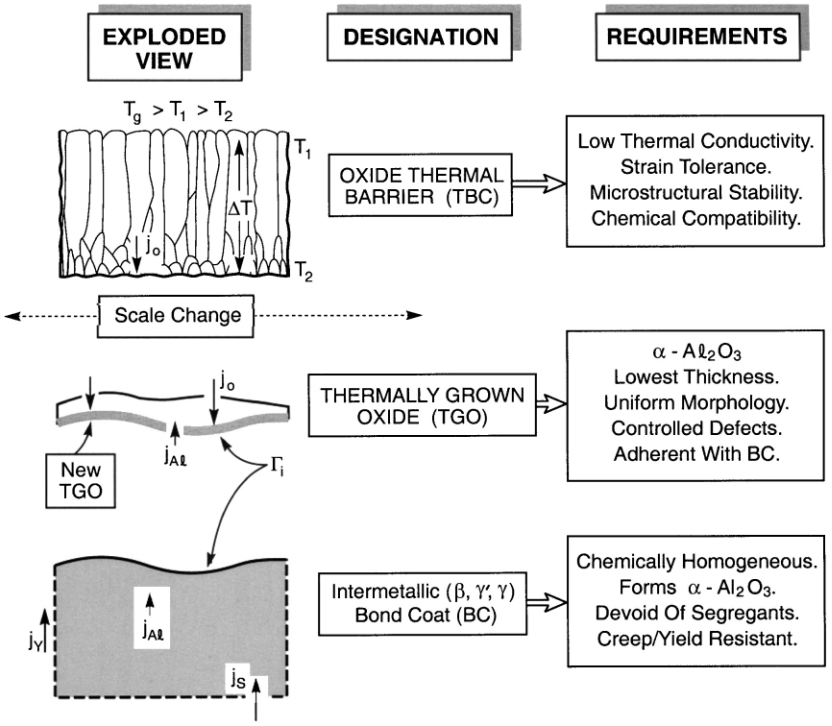

Fig. 2. The four major elements of a thermal barrier system: each element changes with exposure/cycling.

transparent to oxygen). Alumina is the preferred oxide because of its low oxygen diffusivity and superior adherence. This layer develops extremely large residual compressions (3–6 GPa, Fig. 4), as the system cools to ambient, primarily because of its thermal expansion misfit with the substrate (Fig. 5, Table 1) [21–27]. Stresses also arise during TGO growth [19,21]. They are much smaller (generally less than 1 GPa),

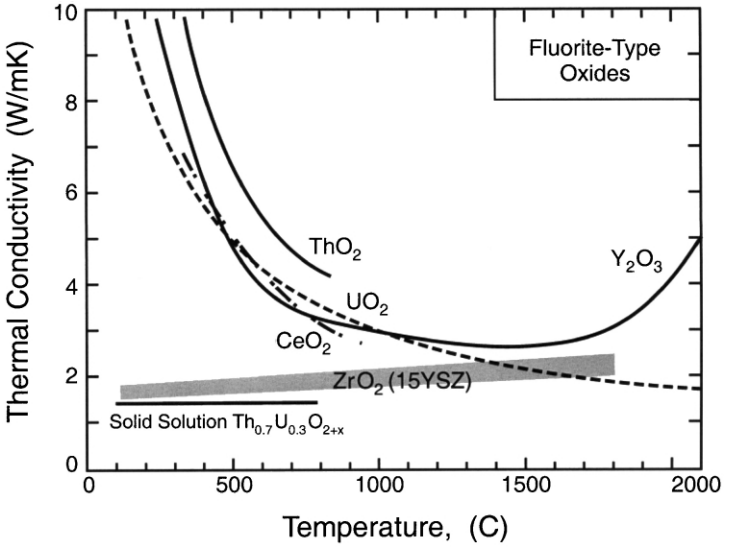

Fig. 3. The thermal conductivity of several insulating oxides illustrating the major role of solid solutions in affecting phonon transport.

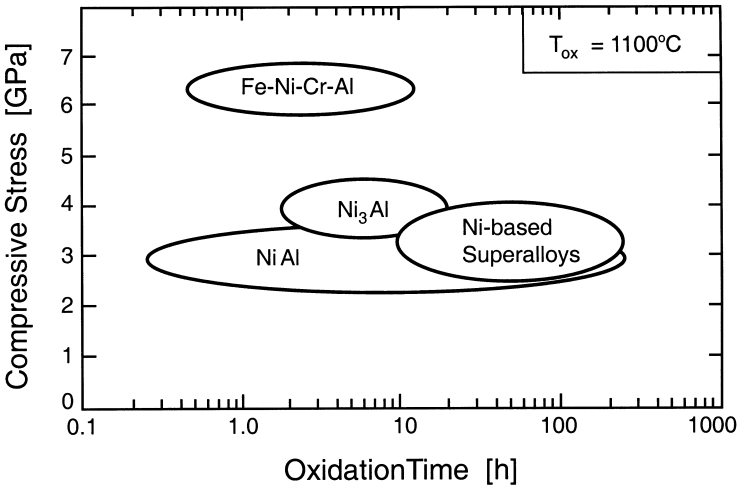

Fig. 4. Ambient residual compressions measured in the TGO developed on several alloy systems (after [21]).

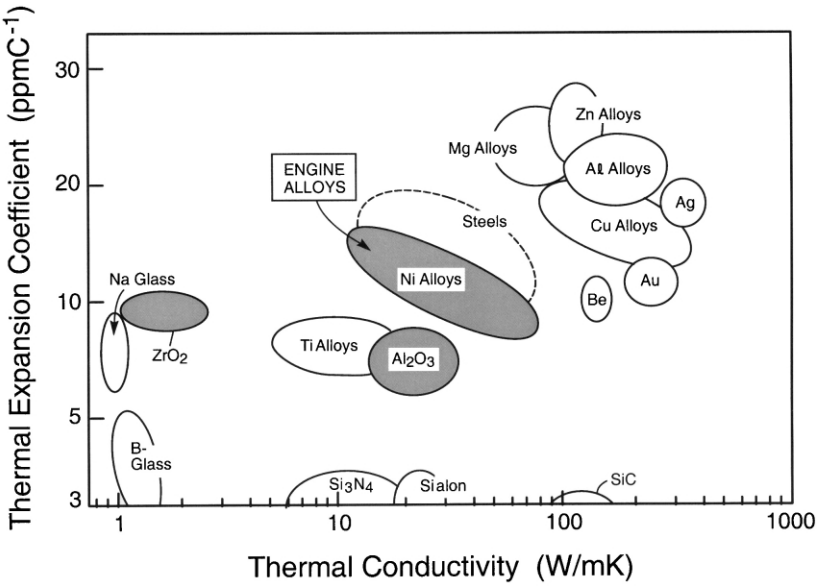

Fig. 5. Cross plot of the thermal expansion coefficient and thermal conductivity of the major material constituents in the TBC system.

Table 1
Summary of material properties

TGO (α-Al_2O_3)	
Young's modulus, E_o (GPa)	350–400
Growth stress, σ^g_{xx} (GPa)	0–1
Misfit compression, σ_0 (GPa)	3–4
Mode I fracture toughness, Γ_0 (J m^{-2})	20
Thermal expansion coefficient, α_o (C^{-1} ppm)	8–9
Bond coat	
Young's modulus, E_s (GPa)	200
Yield strength (ambient temperature) σ_Y (MPa)	300–900
Thermal expansion coefficient, α_s (C^{-1} ppm)	13–16
Interface (α-Al_2O_3/bond coat)	
Mode 1 adhesion energy, Γ^0_1 (J m^{-2})	
Segregated	5–20
Clean	>100
TBC (ZrO_2/Y_2O_3)	
Thermal expansion coefficient, α_{tbc} (C^{-1} ppm)	11–13
Young's modulus, E_{tbc} (GPa)	0–100
Delamination toughness Γ_{tbc} (J m^{-2})	1–100

but still important. Though thin (3–10 μm), the high energy density in the TGO motivates the failure mechanisms discussed in Section 3.

The bond coat is arguably the most crucial component of the TBC system. Its chemistry and microstructure influence durability through the structure and morphology of the TGO created as it oxidizes [19]. Moreover, system performance is linked to its creep and yield characteristics. Bond coats are in two categories. *One is based on the NiCoCrAlY system,* typically deposited by low-pressure plasma spraying (LPPS). It is usually two-phase [β-NiAl and either γ-Ni solid solution or γ'-Ni_3Al]. The γ/γ' phases have various other elements in solution. The Y is added at low concentrations to improve the adhesion of the TGO, primarily by acting as a solid state gettering site for S [28–31], which diffuses up from the substrate. In some cases, small amounts of a Ni–Y intermetallic may also be present. *The second category consists of a Pt-modified diffusion aluminide*, fabricated by electroplating a thin layer of Pt onto the superalloy and then aluminizing by either pack cementation or chemical vapor deposition. These coatings are typically single-phase-β, with Pt in solid solution [19]. Their composition evolves during manufacture and in-service. Diffusion of Al into the substrate results in the formation of γ' at β grain boundaries [19].

The interface between the TGO and bond coat is another critical element. It can be embrittled by segregation, particularly of S [28–31]. During thermal exposure, S from the alloy migrates to the interface. Dopant elements present in the BC getter much of this S and suppress (but not eliminate) the embrittlement. As already noted, bond coats based on NiCoCrAl contain Y for this purpose. The Pt–aluminide BCs do not contain elements which getter S. Nevertheless, they are durable and can have longer lives in cyclic oxidation than NiCoCrAlY systems [30]. While it has been proposed that the Pt mitigates the effects of S [31], there is no fundamental reason to expect this. A number of effects of Pt on the behavior of Pt-modified aluminides have been documented [32] but a complete understanding of the "Pt effect" is an important goal for future research.

A systems approach to TBC design and performance requires that several basic bifurcations be recognized and characterized. Three of the most important are addressed.

i. The NiCoCrAlY and Pt–aluminide bond coats result in distinct TGO characteristics as well as differing tendencies for plastic deformation. Accordingly, the failure mechanisms are often different.

ii. TBCs made by APS and EB-PVD are so disparate in their microstructure, morphology and thermo-physical properties that different failure mechanisms apply.

iii. The failure mechanisms may differ for the two predominant areas of application (propulsion and power generation), because of vastly different thermal histories. Systems used for propulsion and for power peaking experience multiple thermal cycles, whereas most power systems operate largely in an isothermal mode with few cycles. The frequency affects coating durability.

1.2. Failure phenomena

1.2.1. Generalities

Thermal barrier systems exhibit multiple failure mechanisms. Some of the most prevalent are indicated in Fig. 6. (i) In some cases, spinels form either between the

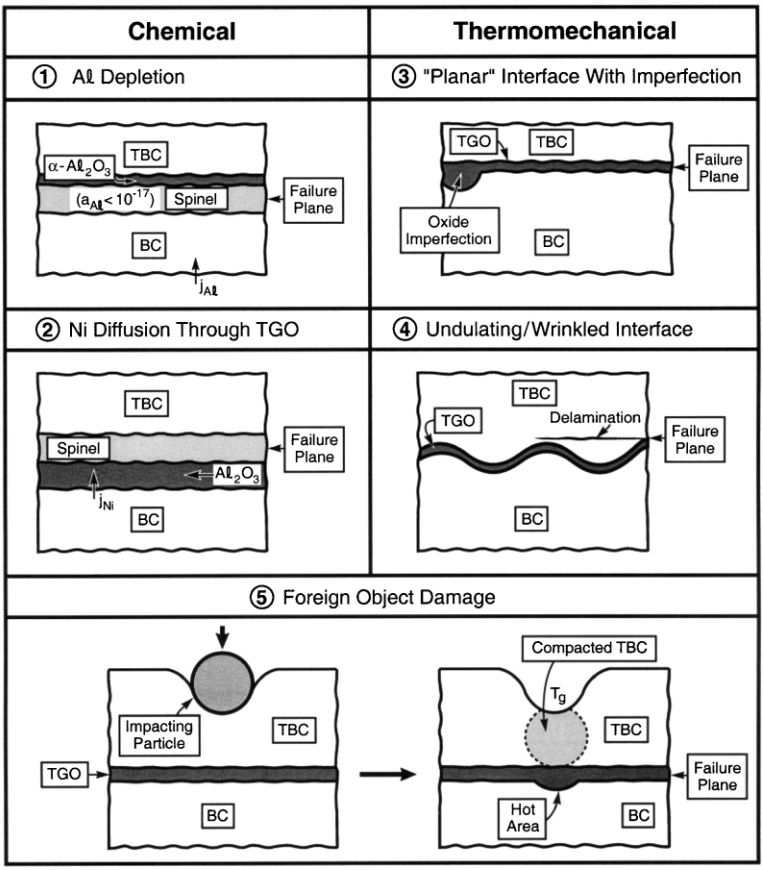

Fig. 6. Five of the major failure categories documented for TBC systems.

TGO and the bond coat or between the TGO and TBC [19]. When this happens, it is surmized (but not substantiated) that the "brittleness" of the spinel results in delamination. (ii) In other instances, regions of the component are subject to particle impact and foreign object damage (FOD) that locally compresses the TBC, resulting in hot spots in the underlying bond coat that contribute to failure [33]. Neither of these failure modes is addressed in this article. Instead, the emphasis is on the third category, (iii) wherein the energy density in the TGO and imperfections in its vicinity (Fig. 7) govern durability. This failure process occurs through a sequence of crack nucleation, propagation and coalescence events [8,24–27,34–38]. Prototypical sequences sketched in Fig. 8 will be elaborated in Section 3. These three elements, while analogous to the stages of cyclic failure in structural alloys [39], have the following special features: (a) Small cracks and separations *nucleate at imperfections* in (or near) the TGO. The tensile stresses that arise around these imperfections and the associated energy release rates govern the details. (b) Once nucleated, the *small*

cracks extend and coalesce, but the TBC may remain attached at remnant ligaments. (c) Failure happens when the ligaments are detached over a sufficient area that a separation becomes large enough to create either a large-scale buckle (designated LSB) or an edge delamination that eventually spalls from the substrate (see Fig. 20) [40].

1.2.2. Specific mechanisms

The specific ways in which the cracks nucleate and grow relate to the increase in the severity of the imperfections as the system is exposed and cycled. While this occurs in many ways, all are ultimately linked to the magnitude and scale of tensile σ_{zz} stresses that amplify as either the TGO thickens or the imperfections increase in size, or both. In turn, the stresses translate into stress intensity factors acting on

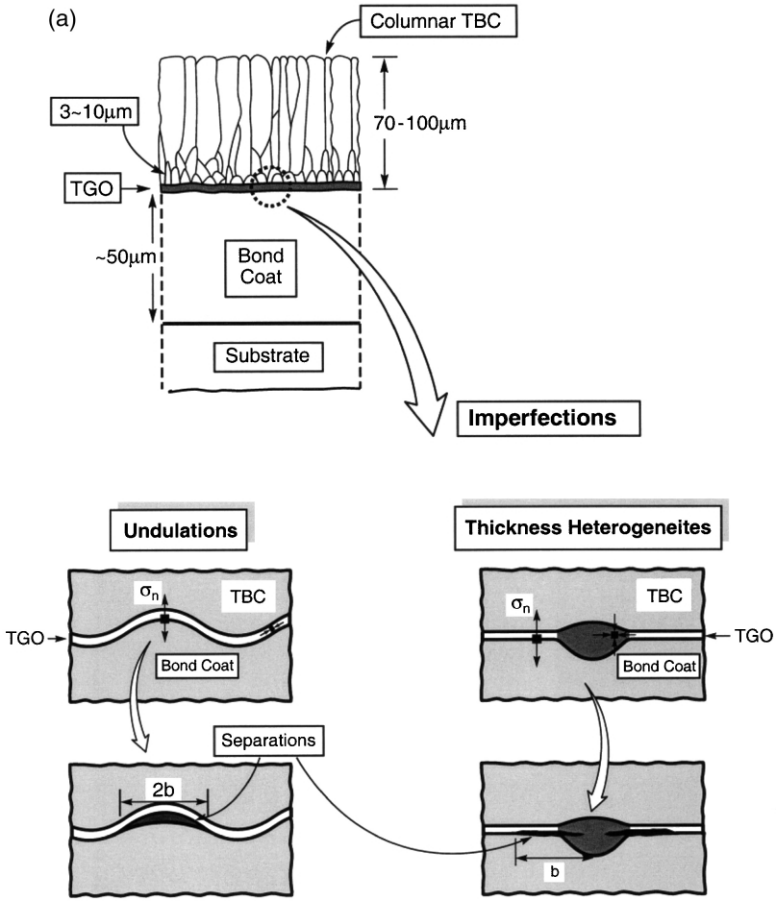

Fig. 7. (a) A schematic of two major categories of TGO imperfection that govern the TBC failure sequence; (b) a thickness imperfection in a TGO grown on a NiCoCrAlY bond coat; (c) an undulation imperfection that develops in a Pt–aluminide system upon thermal cycling.

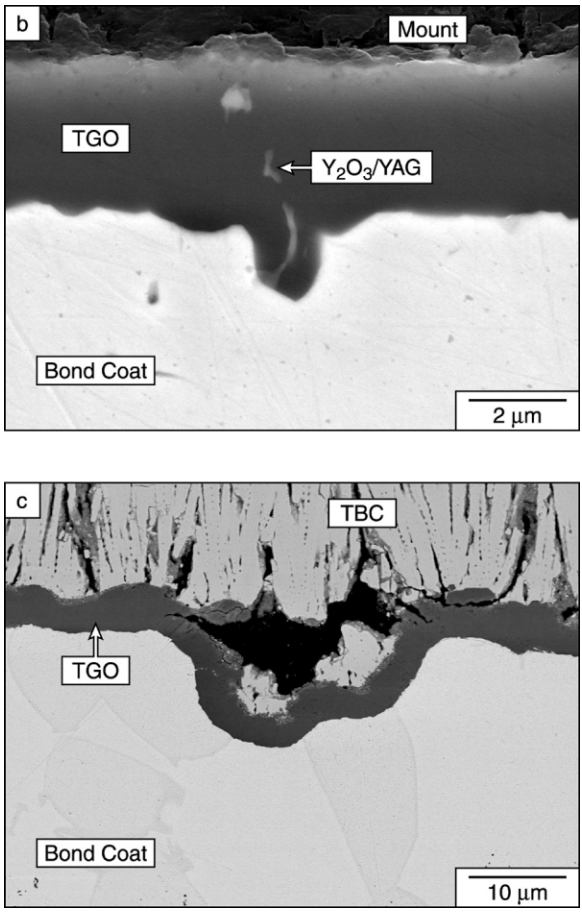

Fig. 7 (*continued*).

cracks that nucleate and propagate around the imperfections [41]. The examples presented in Fig. 8 illustrate the effects of increasing the TGO thickness and of enlarging the imperfection, respectively. Detailed analyses of these mechanisms are summarized in Section 3.

1.2.3. Related observations

After spalling of the TBC from the substrate, the exposed surfaces exhibit two broad morphological categories [19,42]. These observations must be consistent with the failure mechanisms.

i. One predominates for NiCoCrAlY bond coats with EB-PVD TBCs. In such systems, the exposed surface on the substrate side comprises predominantly bond coat with an imprinted TGO grain morphology [42] (Fig. 9a). The exposed surface on the TBC side consists of the TGO with a granular appearance that mirrors the imprint in the bond coat (Fig. 9b). Morphological imperfections in the TGO are

also in evidence. Most prominent are small (about 10 μm) polycrystalline oxide domains embedded in the bond coat [42]. They contain cleavage facets, indicating that they were mechanically detached from the TGO. There are corresponding features on the underside of the TGO.

ii. In other systems, especially those where the TBCs were deposited by the air plasma spray process, a substantial proportion of the delamination traverses the

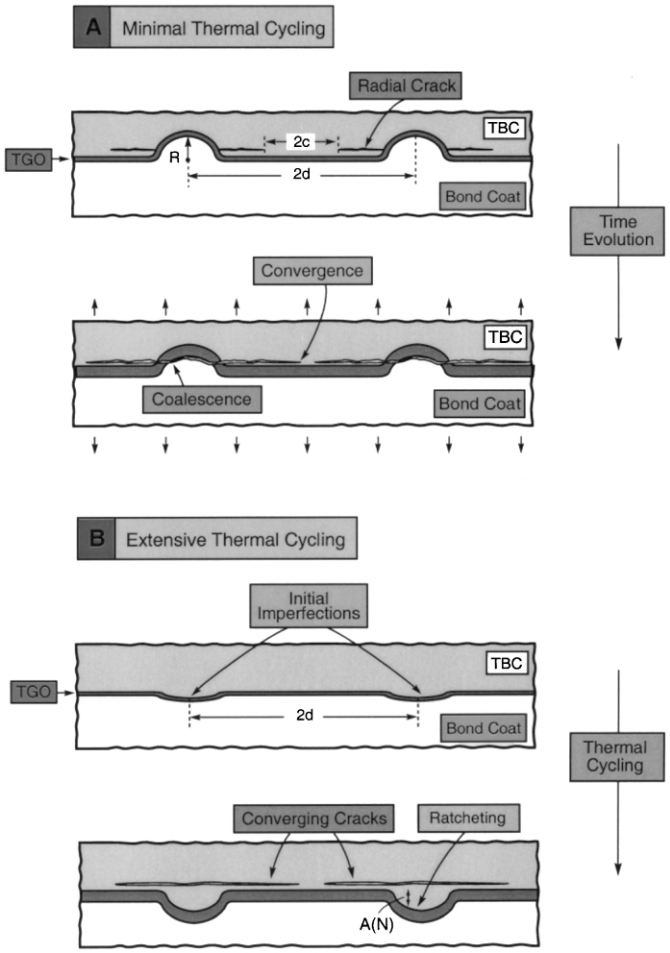

Fig. 8. Two examples of early and late stages of failure from imperfections: (a) schematic of a mode exhibited for scenarios subject to minimal thermal cycling showing how cracks can initiate in the TBC isothermally, due to the growth stresses, and then coalesce with an interface. Separation occurs upon cooling because of the thermal expansion misfit; (b) schematic of the growth of imperfections by ratcheting upon thermal cycling; (c) micrograph of an actual cross section of an APS TBC system highlighting the imperfections [44]. Cracks are in evidence near these imperfections; (d) cross-sections of an EB-PVD TBC on a Pt–aluminide bond coat showing the imperfections that enlarge by ratcheting and the cracks induced in the TBC [82].

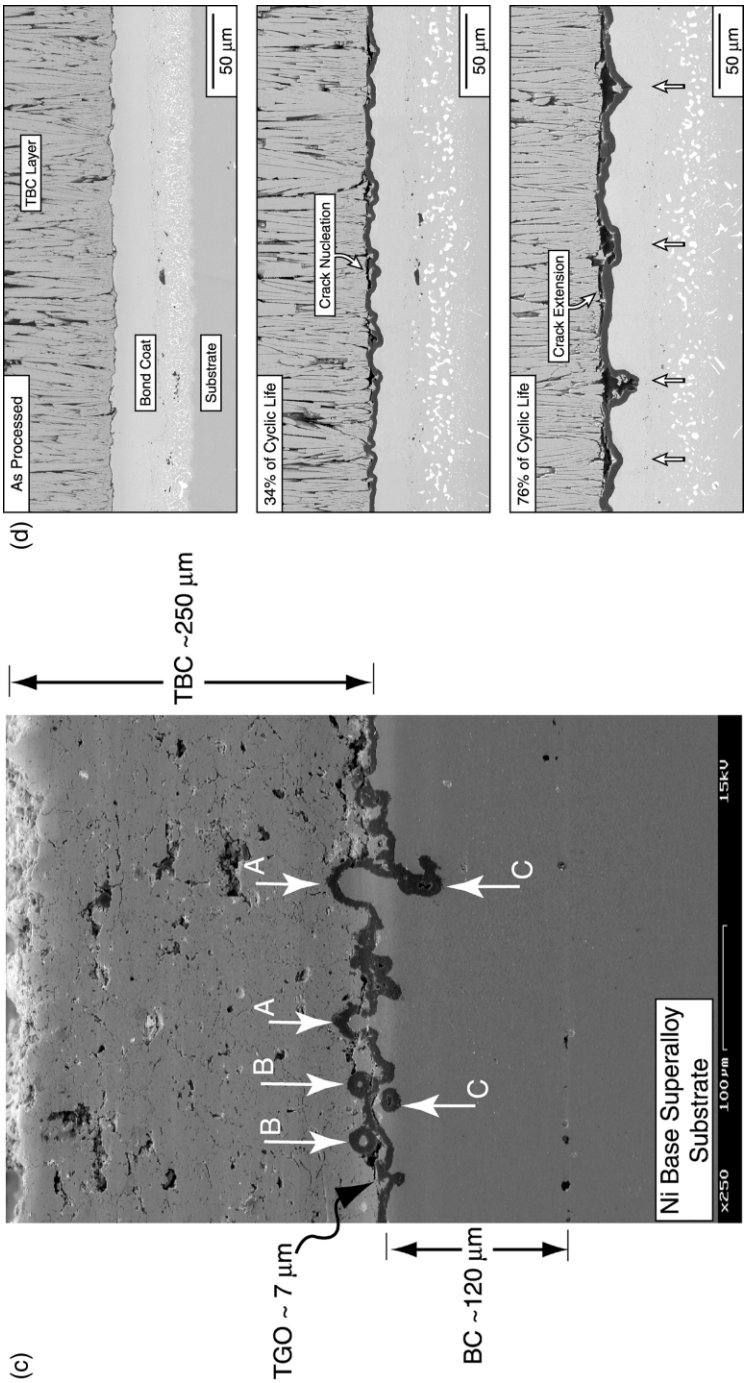

Fig. 8 (*continued*).

TBC itself, with local segments entering the TGO as well as the interface with the bond coat [44]. This mixed appearance diminishes the utility of such observations for interpreting failure mechanisms.

1.3. Overarching principles

Based on the above considerations and on detailed analyses to be elaborated below, the following three overarching principles govern the failure of TBC systems, as sketched in Fig. 10.

i. The TGO experiences large in-plane compressions, especially upon cooling. As with any compressed thin film, it attempts to alleviate the stress (and associated strain energy density) by lengthening itself, through out-of-plane displacements. This can happen by buckling as well as by visco-plastic deformation of the bond coat. These displacements induce tensile σ_{zz} stresses normal to the interface that motivate delamination mechanisms.

ii. When imperfections exist (or are developed) around the TGO, tensions are induced normal to the TGO/bond coat interface, as well as in the TBC, that nucleate and grow cracks in this vicinity. The coalescence of these cracks leads to failure.

iii. The TBC, despite its compliance, has sufficient stiffness to suppress small scale buckling (SSB) of the TGO. Accordingly, eventual failure often occurs by large scale buckling (LSB) [40], but only after a sufficiently large separation has developed near the interface, typically several mm in diameter. The durability of the TBC is governed by the time/cycles needed to develop such separations: through a nucleation, propagation and coalescence sequence, involving the energy density in the TGO, as well as the size and spacing of the prominent imperfections.

2. Thermally grown oxides

2.1. Growth phenomena

While the mechanisms of alumina formation prior to Al depletion are not quantitatively comprehended, especially in the presence of a TBC, the following four findings are pertinent.

i. The growth is essentially parabolic until spalling occurs:

$$h^2 = 2k_p t \tag{1}$$

where h is the thickness, t time and k_p the parabolic rate constant (Table 1). Accordingly, growth is diffusion (rather than interface) controlled. The alumina grows predominantly by inward diffusion of anions along the TGO grain boundaries but there is a contribution to k_p by outward diffusion of cations. This outward growth appears to be sensitive to cations dissolved in the alumina.

ii. In some cases, θ-alumina forms first, particularly on β-NiAl, and transforms to α-Al_2O_3 [45,46]. The θ-phase has an acicular morphology, indicative of growth by

outward diffusion of Al [47]. This morphology is retained upon transformation. The subsequent growth of α-Al_2O_3 appears to be unaffected by the prior transformation.

iii. In some case, the TGO formed on NiCoCrAlY bond coats entrains yttria [42]. The yttria in the TGO is related to the distribution of the Y in the bond coat. When yttria domains of sufficient size are incorporated into the TGO, it thickens more rapidly in these regions and produces thickness imperfections (see Fig. 7). Simultaneously, the yttria reacts with the surrounding alumina to form YAG.

iv. Present the TBC, the TGO may exhibit two distinct microstructural domains: a columnar zone (CZ) next to the BC and an equi-axed zone (EZ) next to the TBC [19]. The EZ found on MCrAlY coatings (which contain Fe), incorporates small (nm) oxide precipitates containing Fe and Cr cations [48], while that on Pt-aluminides comprises a mixture of zirconia and alumina [19].

2.1.1. Thermodynamics

The stability of oxide product phases that form on bond coat materials may be rationalized by constructing thermodynamic stability diagrams. Such a diagram for the Ni–Al–O system is presented in Fig. 11a [19]. This diagram describes the equilibria between the phases in this system (Al_2O_3, $NiAl_2O_4$, NiO and Ni–Al alloys), with the oxygen activity, a_O, as the ordinate and the aluminum activity, a_{Al} (interchangeable with a_{Ni}), as the abscissa. Fig. 11a can be constructed by formulating

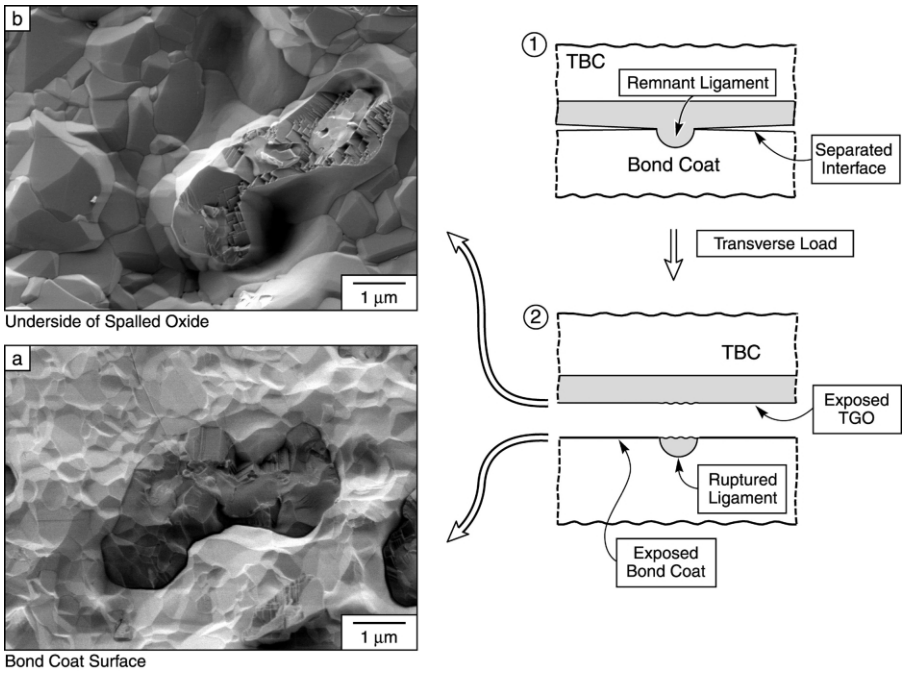

Fig. 9. SEM images of separated interface between a NiCoCrAlY bond coat and a TGO: (a) exposed bond coat; (b) matching surface of the TGO [42].

equilibrium reactions, provided that the standard free energies of formation are available and the activities are understood. The activity of Al in the alloy is related to X_{Al} through the activity coefficient γ_{Al}:

$$\gamma_{Al} = a_{Al}/X_{Al} \tag{2}$$

The activity of Ni is related to that for Al by the Gibbs–Duhem equation:

$$\log \gamma_{Ni} = -\int_{X_{Ni}=1}^{X_{Ni}} \left(\frac{X_{Al}}{X_{Ni}}\right) d\log \gamma_{Al} \tag{3}$$

Accordingly, in order to relate a_{Al} to compositions of the Ni–Al alloys, additional

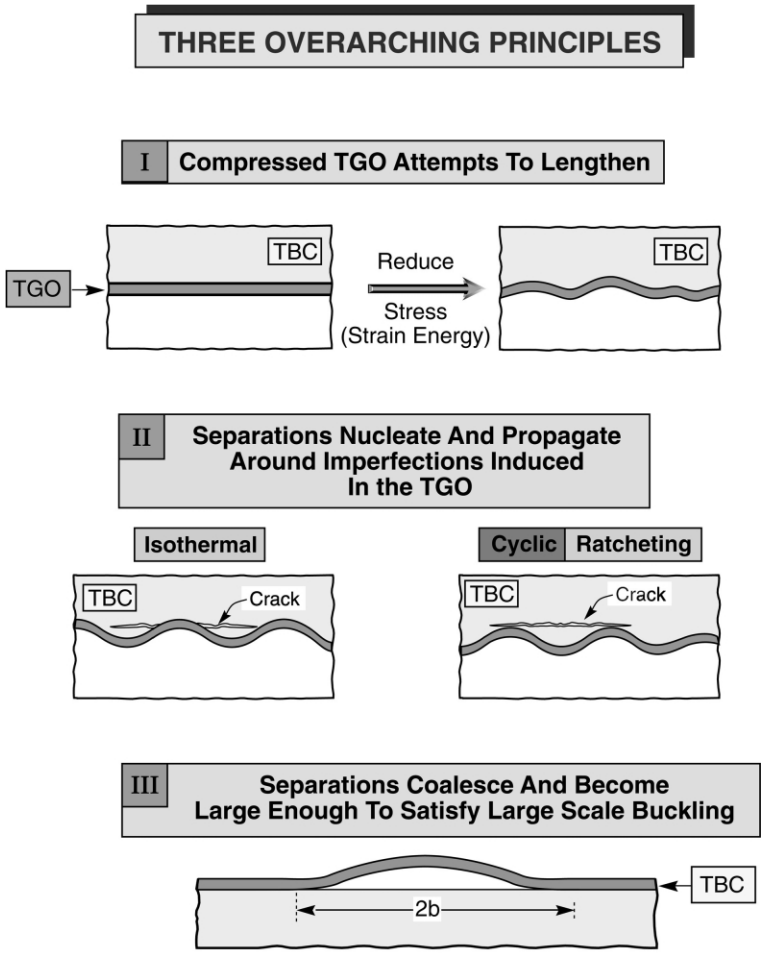

Fig. 10. Sketch illustrating the overarching principles governing TBC failure.

thermodynamic data are required [49] (Fig. 11b). Note that the activity of Al in the alloy is always much less than X_{Al}.

The important equilibria described in Fig. 11a are as follows:

- Line (1) represents Al_2O_3 in equilibrium with Ni–Al alloys through the reaction;

$$2Al(alloy) + 3O = Al_2O_3 \tag{4a}$$

- Line (2) refers to $NiAl_2O_4$ in equilibrium with the alloy via the reaction;

$$Ni(alloy) + 2Al(alloy) + 4O = NiAl_2O_4 \tag{4b}$$

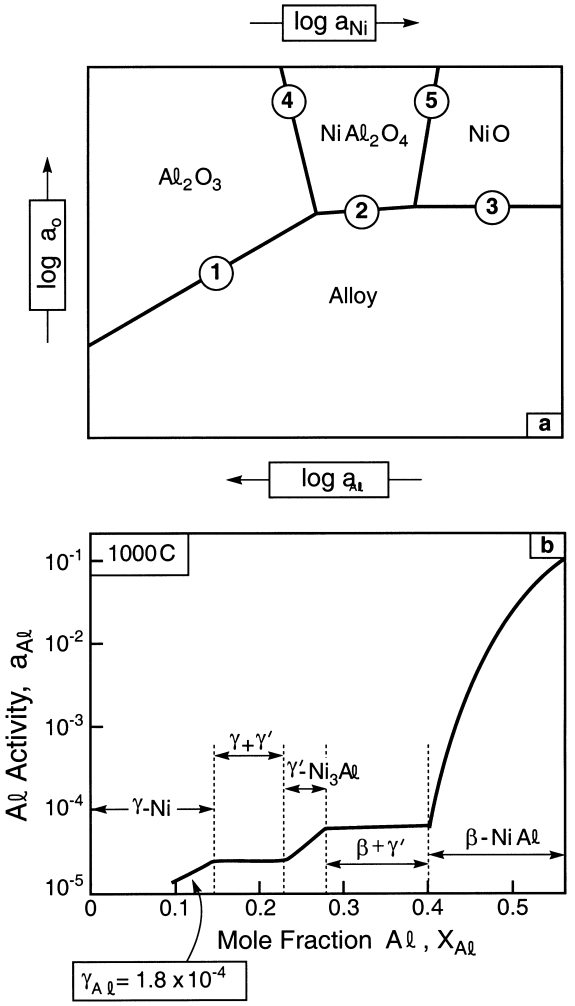

Fig. 11. (a) The thermodynamic stability diagram; (b) the activity coefficient for Al as a function of concentration for the Ni/Al binary [19].

- Line (3) involves NiO in equilibrium with the alloy;

$$\mathrm{Ni(alloy)} + \mathrm{O} = \mathrm{NiO} \tag{4c}$$

The junction of lines (1) and (2) defines a three-phase equilibrium through the reaction;

$$3\mathrm{Ni(alloy)} + 4\mathrm{Al_2O_3} = 3\mathrm{NiAl_2O_4} + 2\mathrm{Al(alloy)} \tag{4d}$$

and the junction of lines (2) and (3), the three phase equilibrium;

$$3\mathrm{Ni(alloy)} + \mathrm{NiAl_2O_4} = 4\mathrm{NiO} + 2\mathrm{Al(alloy)} \tag{4e}$$

The lines (4) and (5) involve two-phase equilibria that can be described through reactions (4d) and (4e), respectively, except that the activities of Al and Ni must be those in the oxide phases.

The stability diagram (Fig. 11a) indicates that at Al activities in the bond coat satisfying $a_{\mathrm{Al}} > 10^{-17}$, reaction (4a) dominates, resulting in $\mathrm{Al_2O_3}$ formation [19]: the thermodynamic situation most favorable for a durable TBC. Whenever $\mathrm{Al_2O_3}$ is stable, the oxygen activity at the interface is too low to form alternative oxides. Upon alumina growth, as the aluminum activity decreases, the oxygen activity at the interface increases along line (1) in Fig. 11a. When a_{O} reaches the intersection of lines (1) and (2), the $\mathrm{Al_2O_3}$ converts to $\mathrm{NiAl_2O_4}$ through reaction (4d). When this happens, the durability of the TBC may be compromised. [For practical bond coats, reaction (4c) never occurs].

Kinetic processes also play a significant role in phase evolution. The effects of kinetics could be included on the stability diagrams by indicating reaction paths, but these kinetics are currently incompletely understood. Two salient findings are as follows [19]:

i. Before a_{Al} in the bond coat decreases to a level that would cause spinel to form, the oxygen flux into the bond coat may exceed the Al flux toward the TGO, whereupon $\mathrm{Al_2O_3}$ precipitates form beneath the TGO in the bond coat.

ii. In some circumstances, as a_{O} at the interface increases, the solubilities of nickel and chromium (as well as Fe when present) in the $\mathrm{Al_2O_3}$ also increase. This condition can result in outward diffusion of cations, through the TGO. Upon encountering higher oxygen activities, these cations can form new oxide phases. For example, in regions between the TGO and the TBC, the thermodynamics and kinetics are such that spinel formation is allowed (Fig. 11a).

2.2. Stresses

The stresses in the TGO exert a central influence on TBC failure. Understanding these stresses is crucial to any model of the durability. There are two main sources of stress: one from the thermal expansion misfit upon cooling and the other from TGO growth [19,21–27,41,50,51]. Both stresses may be alleviated by TGO creep [52–54] and redistributed in the vicinity of imperfections [38,41]. Moreover, the stresses can be substantially modified by thermal cycling conditions that cause cyclic plasticity in the bond coat [37]. Sources of stress development, redistribution and relaxation are

addressed with emphases on the sign and magnitude in the vicinity of imperfections and on the consequences of thermal cycling. Ambient temperature measurements by X-ray diffraction [27] and laser piezo-spectroscopic techniques [21] indicate that thermal expansion misfit results in compressions that, on the average, range between 3 and 6 GPa (see Fig. 4). Direct measurement of the growth stresses by high temperature X-ray peak shift measurements [27,55] indicate that these stresses are also compressive and much smaller than the thermal stresses. They range from near zero for Ni-base alloys to about 1 GPa for FeCrAl(Y) alloys. Nevertheless, they may have an important role in TBC failure. In the vicinity of imperfections the stresses deviate from these average values. Upon thermal cycling, they can even change sign [37]. The specifics are assessed next.

2.2.1. Thermal expansion misfit stresses around imperfections

Imperfections cause the thermal expansion misfit stresses to redistribute. Normal tensions exist where the TGO is concave and vice versa (Fig. 12) [34]. Shear stresses exist at inclined sections. These stresses depend on the elastic mismatch and the ratio of the amplitude A, to the wavelength, L, of the oscillations. When the TGO is thin ($h/L \ll 1$), the stresses are given by [34]:

$$\sigma_{ij}/\sigma_0 = H_{ij}(\alpha_D)A/L \tag{5a}$$

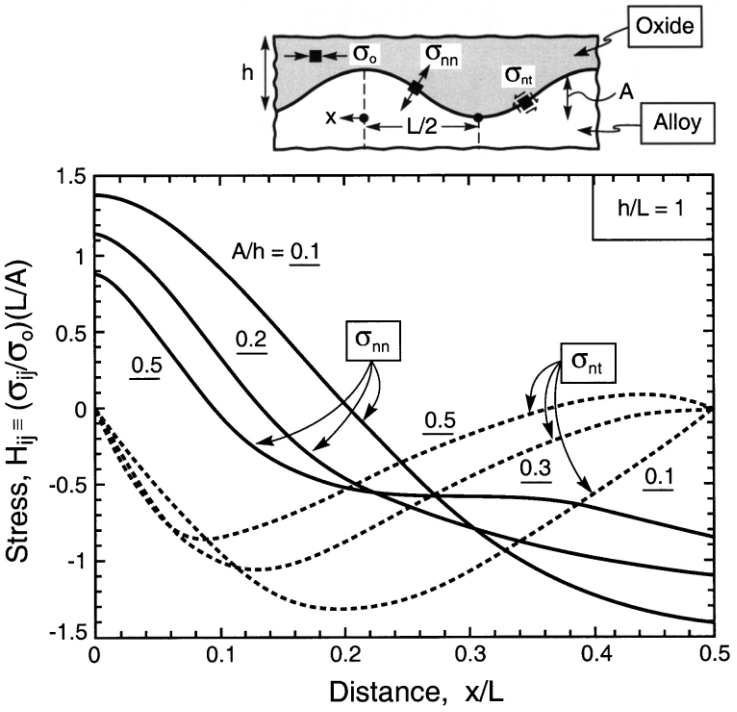

Fig. 12. Distribution of stresses at an undulating TGO interface [34].

where the misfit stress (the stress that would exist in a planar thin film) is [34]:

$$\sigma_0 = E_0 \Delta\alpha_0 \Delta T/(1-\upsilon), \tag{5b}$$

and α_D is the Dundurs' parameter, defined as [56]:

$$\alpha_D = \frac{\bar{E}_1 - \bar{E}_2}{\bar{E}_1 + \bar{E}_2} \tag{5c}$$

with $\bar{E}$ the plane strain Young's modulus and the subscripts 1 and 2 referring to the two adjoining materials. The functions H_{ij} are plotted in Fig. 12. As the TGO thickens, there are additional effects of h/L (Fig. 13).

2.2.2. Redistribution of misfit stresses by bond coat visco-plasticity

The misfit stresses are redistributed by creep or yielding of the bond coat during thermal cycling. Measurements and models characterizing the important effects are developmental [37]. Local misfit stresses around imperfections in the bond coat may become large enough to exceed its yield strength and, thereafter, to induce cyclic yielding. The response may be characterized through a Bree diagram [37,57,58] that identifies domains of elasticity, shakedown and cyclic plasticity (Fig. 14). The specifics are addressed in Section 3. Some elaboration is also given in Appendix E. The coordinates of this diagram are the undulation amplitude-to-wavelength ratio, A_0/L and the misfit stress, σ_0, relative to the bond coat yield strength σ_Y. When these coordinates reside in the elastic domain, yielding is prohibited and the stresses in the

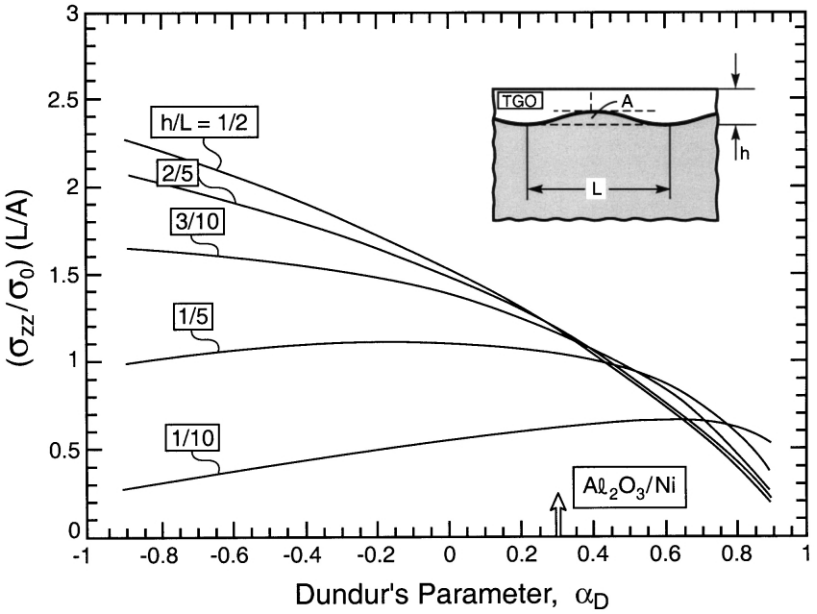

Fig. 13. The effect of elastic mismatch on the stress normal to the interface [34].

TGO are given by the above elasticity solutions. When the bond coat yield strength is exceeded, the stresses are redistributed such that the ambient compressive stress in the TGO is reduced (Fig. 15). Moreover, upon re-heating, regions of tensile stress may develop. These stresses tend to relax by creep (discussed below) but, in some cases, may cause the TGO to crack. In subsequent cycles, the stresses are "reset" by the plasticity that occurred in the first cycle [37]. The response thereafter depends on whether the system is within the "shakedown" or "cyclic plasticity" domain (Fig. 14). In the former, the system becomes elastic after a few cycles and, thereafter, the stresses vary linearly with temperature between the new limits established in the first cycle. Outside this range, the stresses are non-linear and exhibit hysteresis, with consequences for fatigue of the bond coat.

While further changes in the TGO stress may arise when growth strains are added to the thermal expansion misfit, the effect is relatively small, because of the equilibrating influence of bond coat yielding [37]. However, as discussed later, when ratcheting conditions are satisfied, the displacements of the TGO into the bond coat have a major effect on TBC failure.

2.2.3. Growth stresses

Oxidation is accompanied by growth strains and associated stresses [37,59,60]. The strain represents the overall volume increase upon converting the alloy to Al_2O_3. It comprises normal, m_{zz}, and in-plane, m_{xx}, components that depend on the growth mechanism and the induced stresses. In general it can be expressed in the form:

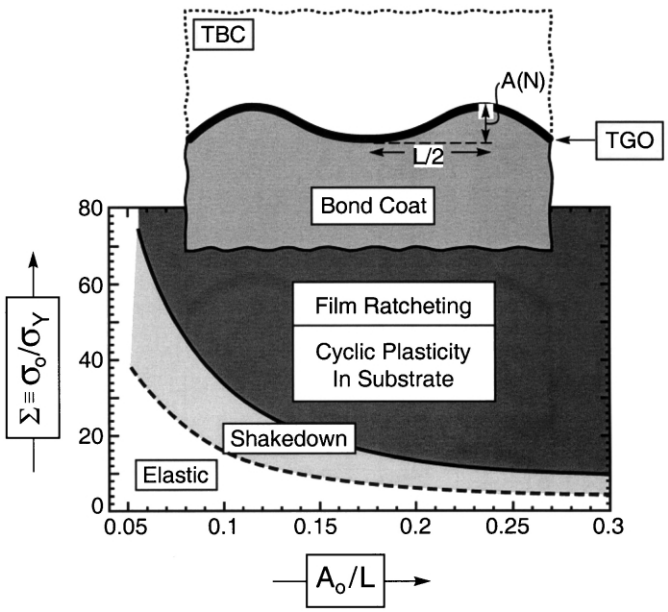

Fig. 14. Bree diagram for a TGO governing ratcheting and shakedown [37].

$$m_{zz}\left(\sigma_{xx}^{g}\right) + 2m_{xx}\left(\sigma_{xx}^{g}\right) = m \tag{6}$$

where σ_{xx}^{g} is the in-plane stress induced by the lateral growth strain. The fundamentals of the growth are incompletely understood. Formation of the new TGO at the interface with the bond coat results in m_{zz} thickening strains with a corresponding rigid body displacement [59,60]. Lateral strains are induced in proportion to that fraction, β, of the new Al_2O_3 that forms, internally, on grain boundaries normal to the interface (Fig. 16). These strains induce σ_{xx}^{g} compressions. When large enough, this stress suppresses internal TGO formation. This happens at a critical stress [59]:

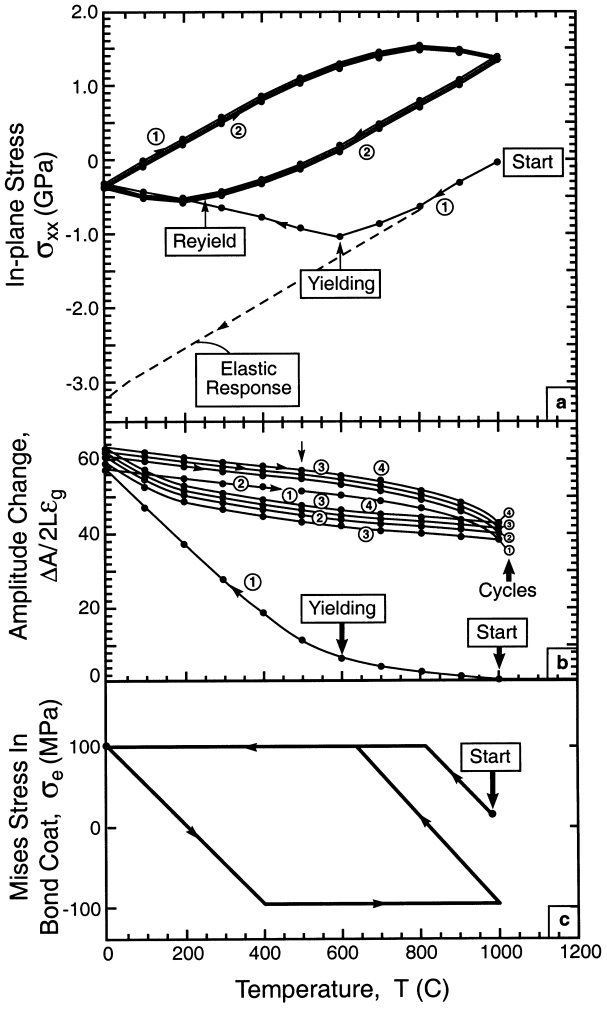

Fig. 15. The evolution of stresses and amplitudes when thermal cycling causes ratcheting: (a) stress in the TGO; (b) the change in the amplitude of the imperfection; (c) the Mises stress in the bond coat [37].

$$\sigma_* = -\left\{\frac{kT\ \ln[p^{g}_{O_2}/p^{eq}_{O_2}][1+1/(1+2(h/g))]}{24\Omega_{Al_2O_3}}\right\} \tag{7}$$

where g is the grain size of the TGO. Inserting typical values indicates a stress of order [59]: $\sigma_* \approx -3$ GPa. In all cases, the measured growth stresses are smaller than this, because the creep strength of the TGO is exceeded (discussed next). Ultimately, the stress levels are established by the creep characteristics.

Information about β and its effect on growth stresses can be gained from direct measurements on thick substrates [19,21,23,26,27,55], as well as from the extension of thin bond coat coupons as they oxidize [22]. On thick substrates, as the stress intensifies, creep

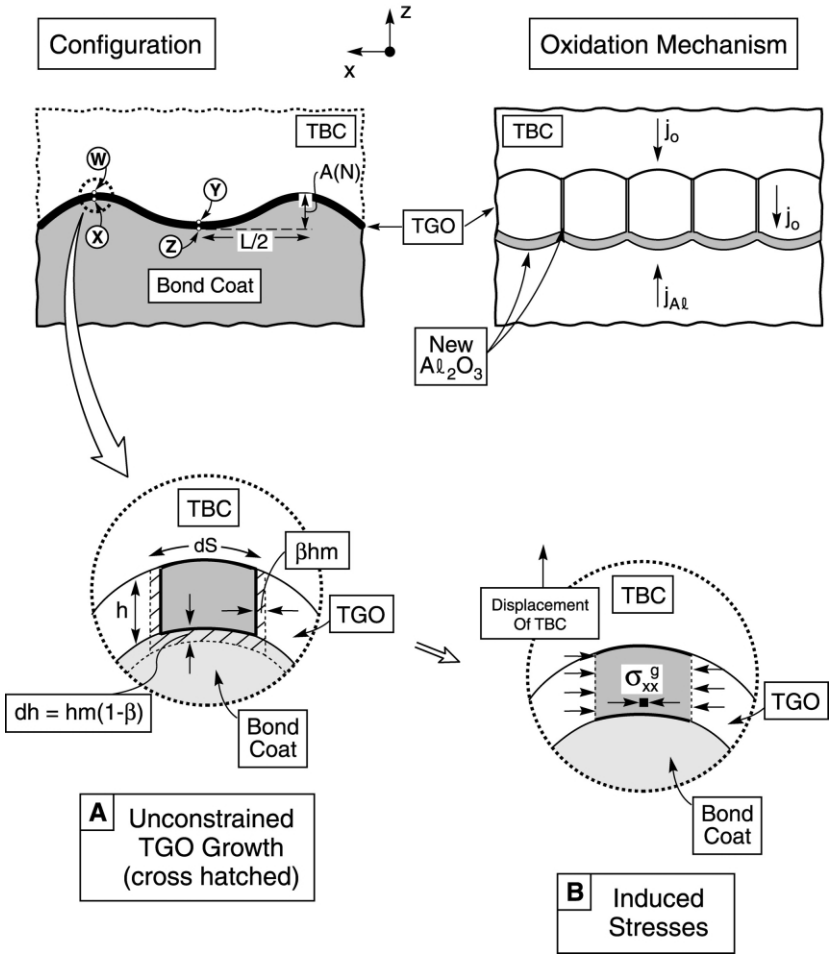

Fig. 16. Schematic indicating the TGO growth modes and its implications for the development of growth stresses.

relaxation ensues, and a dynamic equilibrium exists. This balance results in a "steady-state" growth stress, σ^{g}_{xx} (Appendix C). Within the creep formalism described below, the internal deposition fraction is implied to be of order $\beta \approx 0.1$. Similar values have been found from coupon tests [22]. It has not yet been possible to predict β from basic understanding of oxidation and creep. Note that for $\beta = 0$, the growth strains would be entirely normal to the interface such that, on a planar section, the stresses would be zero.

On non-planar segments of the interface, representative of imperfections, the growth stresses are quite different, because the growth normal to the interface cannot be entirely accommodated by rigid body displacement (Fig. 17) [41]. Moreover, the induced stresses differ for anion- and cation-controlled growth mechanisms. The former has been asserted to predominate for a TGO comprising α-Al_2O_3 [22,61–64]. An approximate

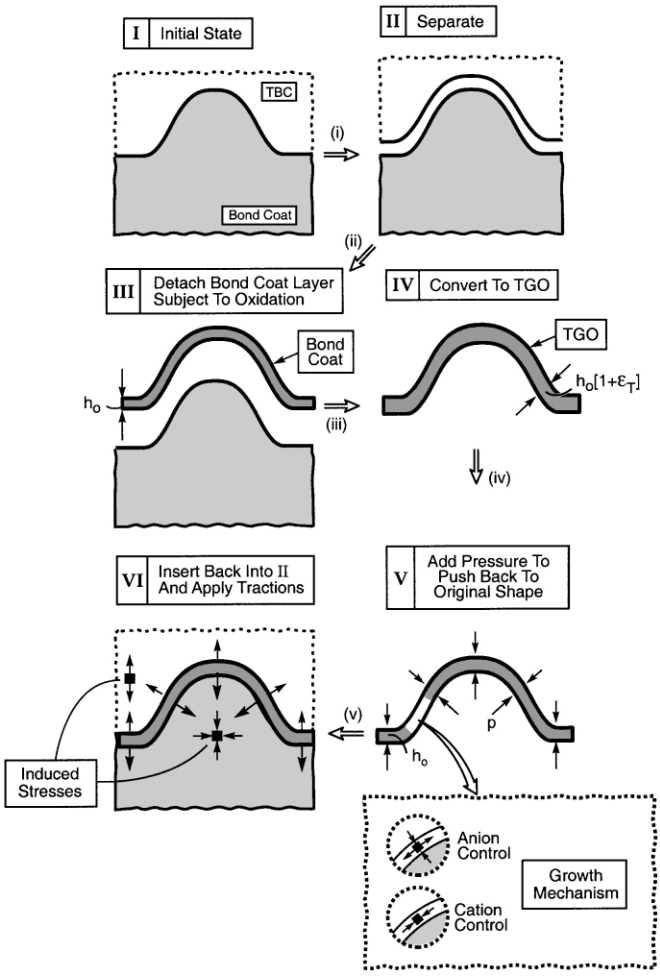

Fig. 17. An "Eshelby" sequence indicating the displacements and stresses that accompany TGO growth [41].

analytical model for a concave imperfection (Appendix B) [37] indicates that the TGO is in hoop tension and radial compression. These stresses have particular importance for cyclic failure mechanisms that involve ratcheting, as discussed in Section 3.

2.2.4. Creep relaxation

At the same temperatures that allow the TGO to thicken by oxidation it experiences creep, because grain boundary transport of anions and cations is involved in both phenomena. Experience with the creep of bulk polycrystalline α-alumina having equivalent grain size provides a frame of reference. When tested at the relatively low stresses amenable to measurement (about 50 MPa or lower), the bulk material deforms in accordance with the expression [65]:

$$\dot{\varepsilon}_c \equiv \dot{\varepsilon}_0 (\sigma_*/\mu_0)^2 \tag{8}$$

with

$$\dot{\varepsilon}_0 \approx 100\left[\frac{D_b \delta_b \mu}{kT}\right]\left(\Omega_{Al_2O_3}^{2/3}/g^2\right)$$

where g is the grain size, μ the shear modulus, $\dot{\varepsilon}_0$ the reference strain-rate for creep (Table 2), $\Omega_{Al_2O_3}$ the molecular volume of alumina and σ_* a reference stress. The diffusivity, $D_b\delta_b$ is considered to be that for diffusion of Al^{3+} ions along the grain boundaries [52–54]. Additions of yttria at levels characteristic of those found in the TGO reduce $\dot{\varepsilon}_0$ (Table 2) [53,54]. While the mechanism responsible for creep in the TGO may differ (because the stress levels are much higher): nevertheless, first order estimates of creep-rates may be made using (8) (see Appendix C).

2.3. Adhesion

2.3.1. Metal/oxide interfaces

Clean metal/oxide interfaces devoid of reaction products are inherently tough and ductile: toughness exceeding 200 J m^{-2} (Fig. 18) [43,66]. The most vivid manifestation is crack blunting [66], which has been documented for interfaces between α-Al_2O_3 with Ni, Au, Cu, Al and Nb. Such high adhesion is realized even though the metals are polycrystalline and non-epitaxial (that is, despite the interfaces being either incoherent

Table 2
Summary of kinetic parameters

		Temperature (°C)		
		1100	1200	1300
Oxidation coefficient, k_p ($\times 10^{17}$ m^2/s)		3	12	81
Creep-rate coefficient, $\dot{\varepsilon}_0$ ($\times 10^{-7}$ s^{-1})	Pure	5	50	400
	Y-doped	0.25	5	50

or subject to a high density of misfit dislocations). However, broad toughness ranges have been cited. This variability arises because of interfacial contaminants or segregants. The effect is most clearly demonstrated by beginning with a clean interface and systematically infusing a contaminant, whereupon cracks propagate at toughness in the range 2–20 J m^{-2} [67,68] (Fig. 18). Beyond these basics, some interfaces are susceptible to stress corrosion in the presence of moisture: particularly Ni and Au [43]. Indeed, stress corrosion of the TGO/bond coat interface has been documented [24,69].

2.3.2. Mechanics

Two fundamentally important factors distinguish fracture at interfaces from that in homogeneous materials [56]:

i. The elastic property mismatch causes the energy release rate, G, and the mode mixity angle, ψ, to differ from that for homogeneous bodies subject to the same loading. These differences are fundamentally governed by the first Dundurs' parameter [56].

ii. Unlike isotropic solids, cracks may extend along interfaces even when the loading deviates from mode I (i.e. $\psi \neq 0$). Accordingly, the fracture toughness must be specified as a function of ψ. A useful phenomenological relation is [56]:

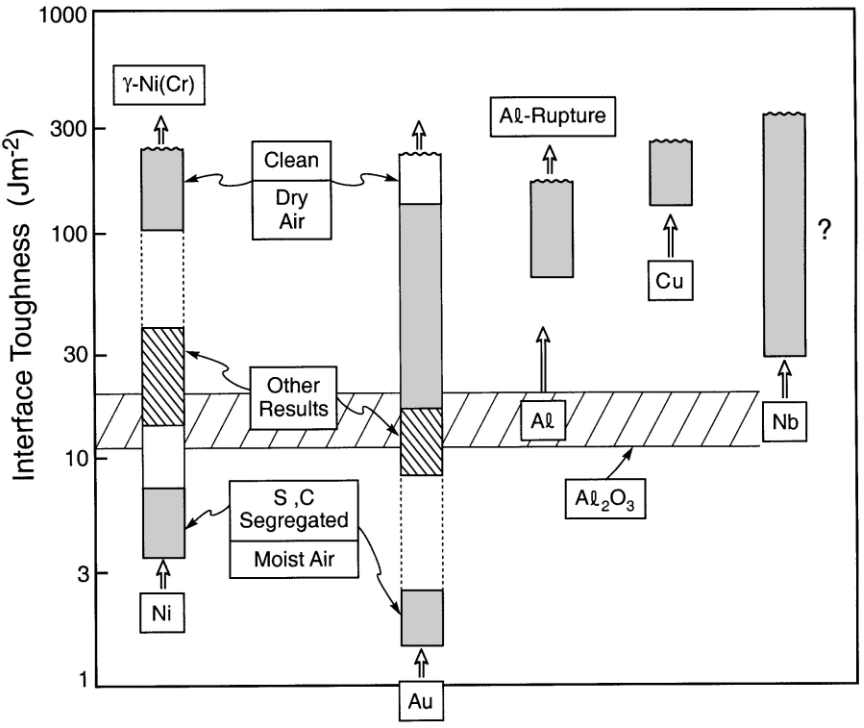

Fig. 18. Summary of experimental measurements of the mode I toughness between α-Al_2O_3 and several metals [43].

$$\Gamma_i = \Gamma_i^0 \tan^2[(1-\lambda)\psi] \tag{9}$$

where Γ_i^0 is the mode I toughness. The parameter λ is a mixity index defined such that there is a strong influence of mode II when λ is small. The effect is crucially important to the understanding of buckling, spalling and cracking [56,70]. Notably, as ψ increases (because of a relatively large shear loading), various responses reduce the displacements that transmit to the interface crack tip. These effects include friction at contacting crack wake asperities, as well as elongated plastic zones in the metal. The consequences include the stabilization of buckles and edge delaminations. One of the major challenges in characterizing interface adhesion is the determination of λ. This is especially true for the TGO/BC interface.

2.3.3. Test protocols

Interface toughnesses for films and coatings on ductile substrates are most readily determined by impression tests [42,71]. They can also be measured by inducing buckle propagation [70] (Appendix A). Impression methods use an indentor with

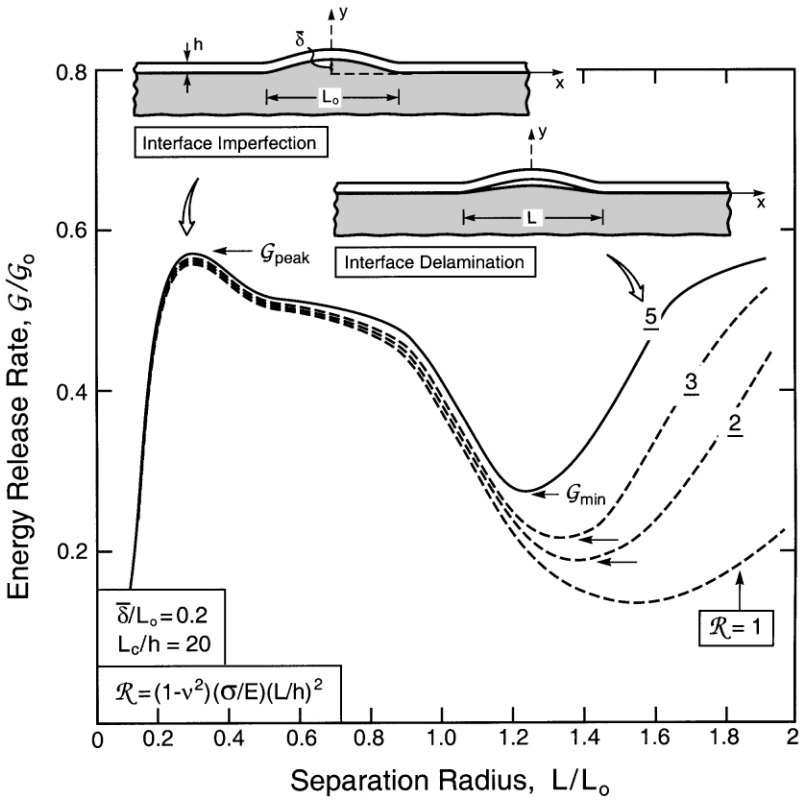

Fig. 19. The variation in energy release rate with separation size for a TGO, absent the TBC, in the vicinity of an imperfection [72].

prescribed geometry to plastically impress the substrate. The impression induces in-plane compressive strains along the surface that vary with distance from its center. These strains are transmitted up into the film. The strain energy density in the film (deriving from both the impression and the thermal expansion misfit) provides the energy release rate. In all cases, G initially decreases with distance from the impression, causing the delamination to develop stably as the impression depth increases.

2.3.4. Measurements

Direct measurements of the toughness of the interface between the TGO and bond coat have been recent and sparse [24,42,70]. Determinations made using the buckling method [24,70] have indicated that $\Gamma_i \approx 5$–10 J m^{-2}, with a mode mixity $\psi \approx 50^\circ$. Such low toughness is characteristic of embrittled Ni/Al_2O_3 interfaces [68] (Fig. 18). Wedge impression and edge delamination measurements performed with the TBC present have provided estimates of the mode II interface toughness: $\Gamma_{i\mathrm{II}} \approx 60$ J m^{-2} [42]. These higher values (relative to the buckling results) reflect the role of interface friction [λ in Eq. (9)].

2.4. Failure

TGO films eventually fail by small-scale, buckle-driven delamination [70] (SSB). Failure is motivated by the strain energy density in the TGO and resisted by the fracture toughness along the delamination plane, usually the interface. Should all of the strain energy be available for decohesion (which it is not), a lower bound for the thickness of the TGO that remains attached, $h_{\min}$, can be specified as [8]:

$$h_{\min} = E_0 \Gamma^0 / \sigma_0^2 (1 - \upsilon) \tag{10}$$

Actual failure phenomena involve a critical TGO thickness, h_c, related to the minimum by:

$$h_c = \xi h_{\min} \tag{11}$$

(with $\xi > 1$). The range expected for $h_{\min}$ is bound by choices made for Γ^0 and σ_0. It is between 70 nm and 1 μm [8], *appreciably smaller than the TGO thickness sustained in practice* (between 3 and 10 μm). The discrepancy arises because there is no mechanism capable of transmitting all of the strain energy into the delamination. Accordingly, mechanisms need to be postulated that transmit some of this energy into a release rate capable of growing a separation to a size large enough to cause SSB and spalling [40]. Imperfections in the TGO exert a major influence on this process [34–38].

In the presence of imperfections, particularly undulations of the surface (see Fig. 7), local tensile stresses are created normal to the interface, large enough and over sufficient spatial extent to cause the formation of well-defined separations. At this stage, the energy release rate G associated with the separation increases to a peak (Fig. 19) [72] and then decreases as it extends, causing it to be stable and self arresting. However, when the separation becomes large enough to satisfy buckling

requirements, opening of the crack occurs, substantially increasing G and resulting in a minimum (Fig. 19) [72]. *The minimum value represents a buckle propagation criticality*. It translates into a critical imperfection wavelength, L_c needed for SSB and ensuing failure [72]:

$$L_c \approx 5h_{min}\sqrt{E/\sigma_0} \tag{12}$$

The above results for h_c and L_c should be interpreted as follows. The combined inequalities, $h < h_c$ and $L < L_c$ represent a fail safe condition. That is, it can be assured that the TGO remains attached, even though separations may be present. However, when one inequality is not satisfied, there is a finite probability that the TGO will fail by SSB.

3. TBC failure mechanisms

Edge and buckle-driven delamination compete as mechanisms of final TBC failure. The failure map (Fig. 20) [40] represents the basic elements of this competition. In the upper right, the TBC has relatively high in-plane stiffness and limited strain tolerance, causing the residual stress in the TBC to be large and resulting in a high strain energy density. This energy density enhances that from the TGO and provides a strong driving force for edge delamination which, in turn, is resisted by the mode II toughness along the most brittle pathway (among the TBC, TGO or interface). In the lower left of the map, the low in-plane modulus of the TBC does not resist small scale buckling of the TGO, whereupon the system would fail under conditions similar to those for the TGO, absent the TBC. At the intermediate levels of in-plane modulus used in practice, SSB and edge delamination are suppressed, and the system resides in a "fail-safe" domain until degradation phenomena operating on either of these mechanisms envelop this domain. This failure map provides a conceptual framework for addressing durability. TBC systems operate within the following two principal domains:

i. When the TBC experiences thermo-mechanical loadings typical of those applicable to "power generation", with long high temperature exposures and minimal thermal cycling, the cracking patterns are dominated by a combination of the TGO growth stresses and those from the thermal expansion misfit.

ii. Loadings representative of aero-engines comprising extensive thermal cycling are more likely to be affected by strictly cyclic phenomena such as ratcheting, wherein cyclic displacements of the TGO into the bond coat set-up the delamination strains in the TBC.

3.1. TBC properties

3.1.1. Stress/strain relationships

Because of the porosity used to achieve strain tolerance, the thermo-physical properties of the TBC are non-linear and complex. They have yet to be adequately

characterized. Stress/strain curves measured on APS material [17] illustrate the predominant features (Fig. 21). The strains are anelastic/hysteretic, characteristic of those found for porous brittle solids and ceramic composites [73]. A generalized representation could be developed on the experience with these analogous materials, but has not yet been established. One useful approach is to express the tangent modulus E_T as a function of the in-plane pre-stress σ_0 [74] (Fig. 22). This representation leads to a "unified" relationship $E_T(\sigma_0)$ that can be used in design or life prediction. As yet, this relationship does not adequately account for either the hysteresis or the permanent strains.

While the use of a single-valued modulus for analyzing the performance of TBCs is clearly an oversimplification, without a fully-developed alternative, presently some judgement needs to be made about the appropriate value when a modulus is needed

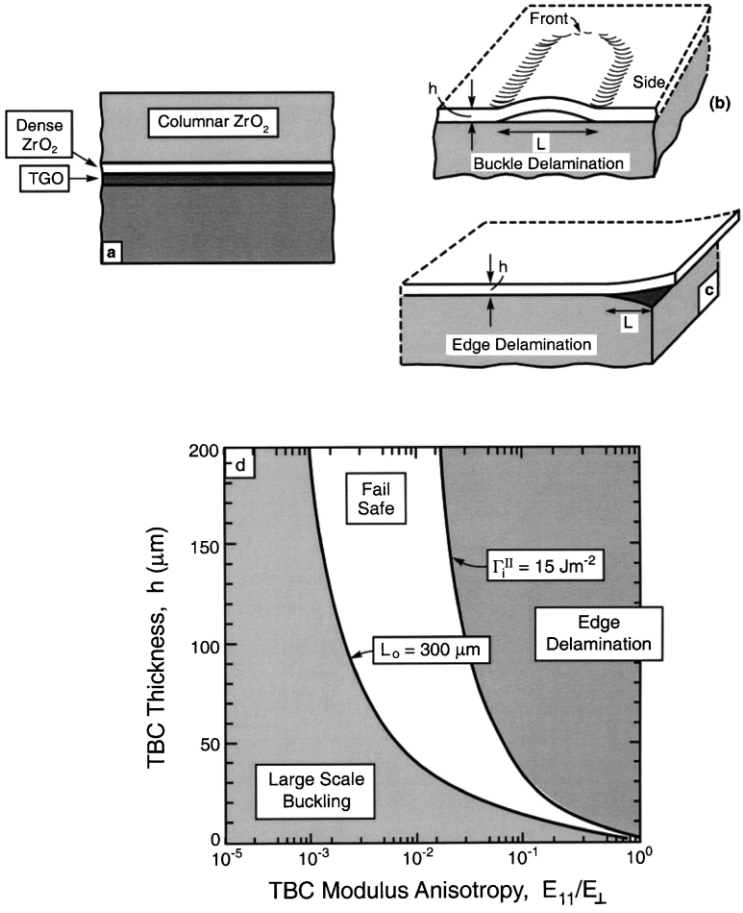

Fig. 20. TBC durability map indicating the domains for large scale buckling and edge delamination [40]. The intervening domain represents a "fail safe" condition. Over time and cycling this domain shrinks and is encompassed by one of the failure mechanisms.

as a parameter in durability models. *A substantial new study is needed to introduce anelastic phenomena in a manner that can be used effectively in a numerical model.*

3.1.2. Fracture resistance

The toughness of the TBC is anisotropic [17,75–78]. It is dependent on the deposition approach and strongly affected by the mode mixity, as well as being a function of crack length (because of short-crack and *R*-curve phenomena). It is also ill-defined, especially in the large crack limit, unless a full non-linear approach is used (such as either the *J*-integral or a large scale bridging algorithm). Given these complexities, plus the difficulty in testing actual coatings, the overall toughness domain is minimally encompassed. A framework for addressing the seemingly disparate measurements is sketched on Fig. 23a, with reference to cracks on delamination planes nominally parallel to the substrate. For short cracks (length in the range, $a \leqslant 100$ μm), the mode I toughness can be quite low. (Subject to the above proviso about the limitations of linear elastic fracture mechanics) the few measurements that have been made (all on APS materials) suggest toughness in the range: $0.1 \leqslant K_{\mathrm{Ic}}^{\mathrm{tbc}} \leqslant 1$ MPa $\sqrt{\mathrm{m}}$

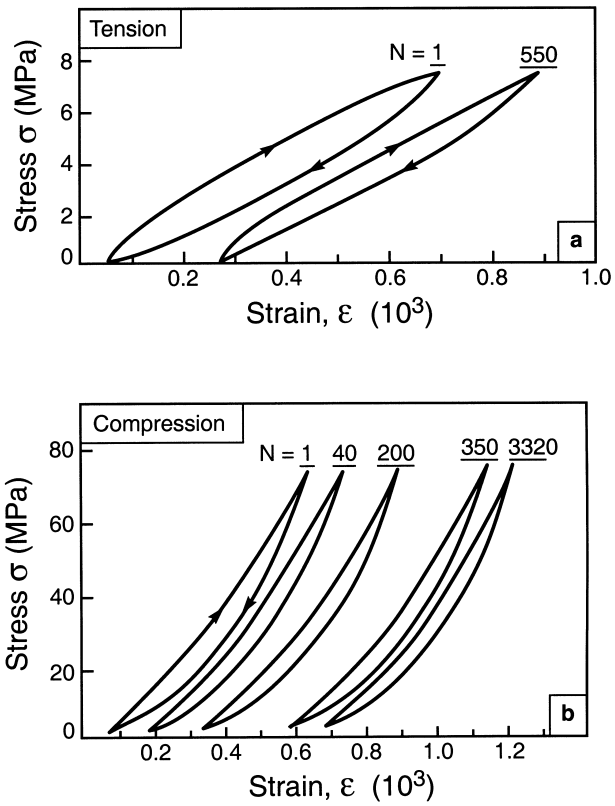

Fig. 21. The non-linear stress/strain characteristics of a TBC. These are derived from the results presented in reference [17].

[17,44]. Such values represent the fracture resistance of splat interfaces. Similar values might be expected for EB-PVD coatings because of the low toughness of t′-ZrO_2.

As the cracks extend, resistance curve behavior arises, particularly in mode II because of the strong influence of crack face friction [79]. For long cracks ($a \geqslant 1$ mm) in mode II, the toughness reaches: $K_{IIc}^{tbc} \approx 3$–$5\,\mathrm{MPa}\sqrt{\mathrm{m}}$ [75–78]. Friction arises in the presence of non-planarities along the crack plane. There are two interacting effects on the toughness. The undulations cause the TBC above the crack to displace upward as it propagates, resulting in elastic strains and associated strain energies that resist crack growth. Additionally, frictional dissipation occurs at the contacting asperities. The coupled effects are plotted in Fig. 23b. Beyond these influences, crack extension is resisted by intact ligaments and/or by microcracking.

3.2. The role of imperfections

Failures are associated with imperfections located at (or near) the TGO layer, especially those that induce tensile σ_{zz} stresses normal to the TBC surface, in the vicinity of the TGO. These stresses, in turn, initiate cracks along trajectories having lowest toughness [19,37]. Often, the important imperfections enlarge with exposure/cycling [37], thereby increasing the nucleation probability while also extending previously formed cracks.

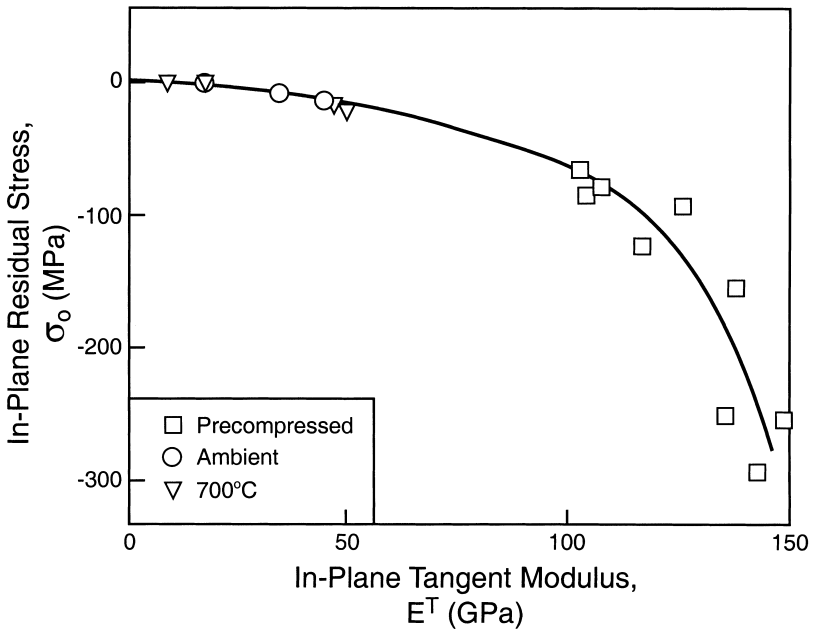

Fig. 22. Cross-plot of the (small strain) tangent modulus as a function of the pre-stress for TBCs [74].

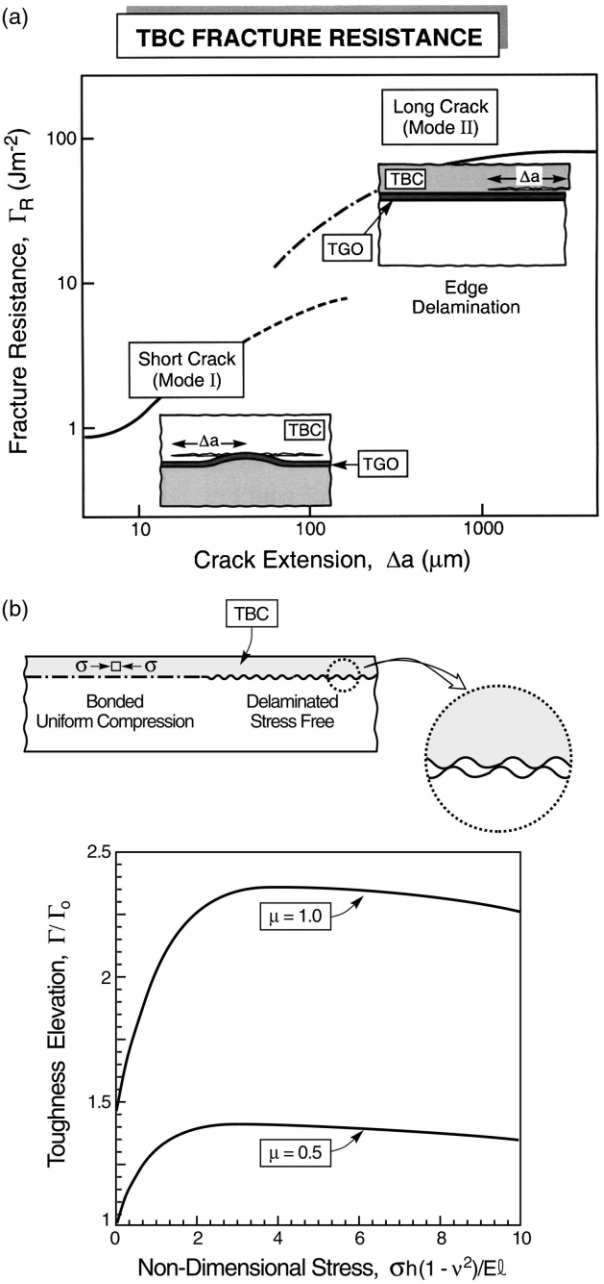

Fig. 23. (a) Schematic of the fracture toughness of TBCs. Short cracks in mode I have toughness in the range, $K_{IR} \approx 0.1 - 1\,\text{MPa}\sqrt{\text{m}}$, with a resistance that increases as the crack extends, because of the material non-linearity. Long cracks in mode II have toughness: $K_{IIR} \approx 5\,\text{MPa}\sqrt{\text{m}}$. This toughness includes contributions from crack face friction. (b) The effects of undulations and friction on the delamination toughness of compressed coatings [79].

There are three key technical challenges toward determining the role of imperfections in failure: (i) ascertaining the mechanisms that enlarge the imperfections, (ii) evaluating the energy release rates at cracks emanating from them and (iii) ascertaining their size and spatial distributions.

Undulations are pervasive imperfections. They emerge as failure origins for two reasons. Under predominantly isothermal conditions, the misfit from TGO growth results in appreciable stresses in the TBC around the imperfections [41]. With extensive thermal cycling, initial undulations in the TGO increase their amplitude upon thermal cycling [37]. This occurs by "ratcheting" of the TGO into the bond coat (Figs. 8 and 24). As the amplitude, A, increases, σ_{zz} stresses develop in the superposed TBC. These stresses ultimately lead to separations large enough to satisfy LSB and, thereafter, TBC failure. There are two main elements:

i. When the shear stresses induced in the bond coat upon cooling sufficiently exceed its yield strength, it flows plastically from the base to the peak of the prominent undulations, allowing the amplitude to increase. This process may continue for a few cycles, but then stabilizes [37].

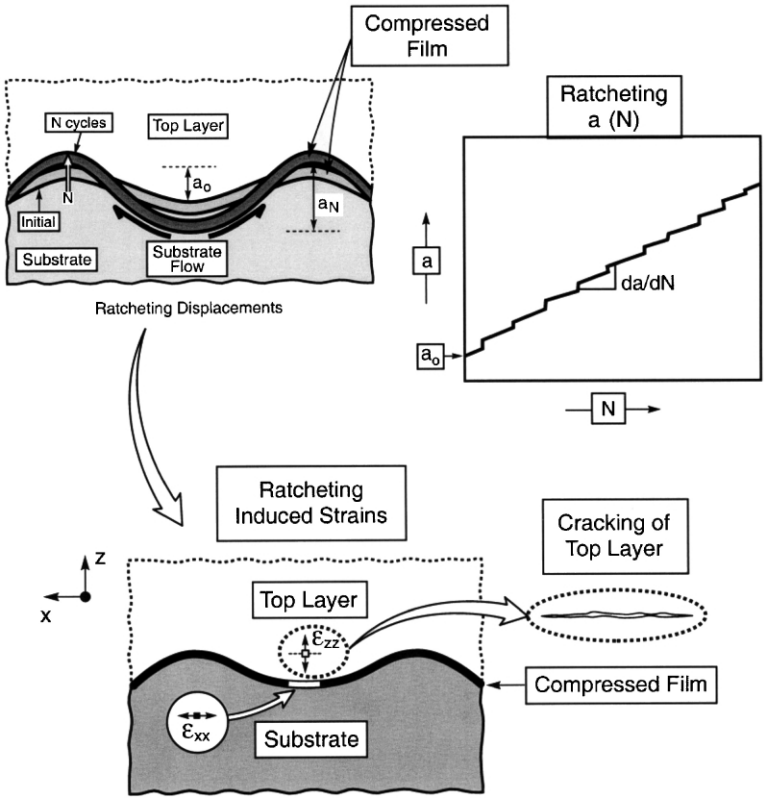

Fig. 24. Schematic indicating the ratcheting phenomenon and the steady-state growth in undulation amplitude that can arise when a critical size has been exceeded [37].

ii. For the undulation to continue to enlarge, the growth strain at high temperature "feeds" the process. In such cases, steady-state ratcheting becomes possible, whereby A increases with each thermal cycle [37] (Fig. 24). These cyclic phenomena are characterized through a modified Bree diagram (see Fig. 14), which shows that, for all intents and purposes, ratcheting initiates at undulations exceeding a critical aspect ratio, A_c/L, dependent on the bond coat yield strength and the TGO growth strain.

TGO thickness imperfections have been suggested as alternative failure nucleation sites [42]. They appear to become important when undulations are suppressed. They form and enlarge in regions where the O^{2-} diffusivity through the TGO is exceptionally large. This happens at locations where the TGO contains oxides other than α-Al_2O_3 having intrinsically lower resistance to O^{2-} diffusion. Examples comprise TGOs that entrain Y from the bond coat to form yttrium aluminates and become locally thick (see Figs. 7b and 9) [42]. Above a critical size, the tensile stresses around these imperfections are predicted to nucleate interfacial separations [72].

3.3. Stresses, cracking and failure

Imperfections are important because of the tensile stresses that develop around them as the TGO grows and the system thermally cycles. The principal focus is on the σ_{zz} stresses, because these are the stresses governing crack growth parallel to the interface, near the TGO. Moreover, σ_{zz} must increase systematically as the TGO thickens to account for its documented influence on TBC failure. In scenarios subject to minimal thermal cycling, σ_{zz} stresses in the TBC are dominated by TGO growth [41], augmented by expansion misfit (Appendix B). Extensive thermal cycling introduces other stresses by ratcheting of the TGO into the bond coat (Appendix E) [37]. The following analyses demonstrate how cracks nucleate and grow from imperfections and render expressions for the crack size. However, for failure to occur, many of these cracks must first coalesce. The practicalities of this are complicated by the residually-compressed remnant ligaments between cracks that experience a vanishing energy release rate at convergence. Ultimately, the detachment of these ligaments governs the onset of large scale buckling (LSB) [40] and failure in accordance with Fig. 20.

Progress is made by adopting the simplifying assumption that adequate transverse loadings are always present (because of inertial motions or vibration), whereupon crack coalescence can be ascribed to a requirement that the crack diameter equal the spacing 2d between neighboring imperfections.

Minimal thermal cycling scenarios, being immune to high cycle phenomena such as ratcheting, have durability governed largely by the stresses that arise upon TGO thickening. Within such scenarios, excursions to ambient are important. The overall cracking scenario is depicted in Figs. 25 and 26 [41,44].

Upon TGO growth around imperfections, the change in volume cannot be fully accommodated by rigid body displacements. The ensuing dilatation induces tangential tension in the surrounding TBC, with consequences for radial cracking (Appendix C). These stresses are unaffected by TGO creep [41].

Upon cooling, the compression normal to the TGO interface diminishes, because of thermal expansion misfit [41,80]. In fact, should the bond coat creep sufficiently during TGO growth, this stress becomes tensile at ambient and motivates interfacial separation. Furthermore, when the TGO exceeds a characteristic thickness, the tangential tensions within the TBC (caused by growth) are enhanced by the expansion misfit (Appendix B) [41,80].

Coalescence of the interface separations with the radial cracks in the TBC, through the TGO, creates a connected crack (Fig. 25c). Such delaminations have stress intensities [Appendix C (C1)] that result in a crack radius, a, given by [41]:

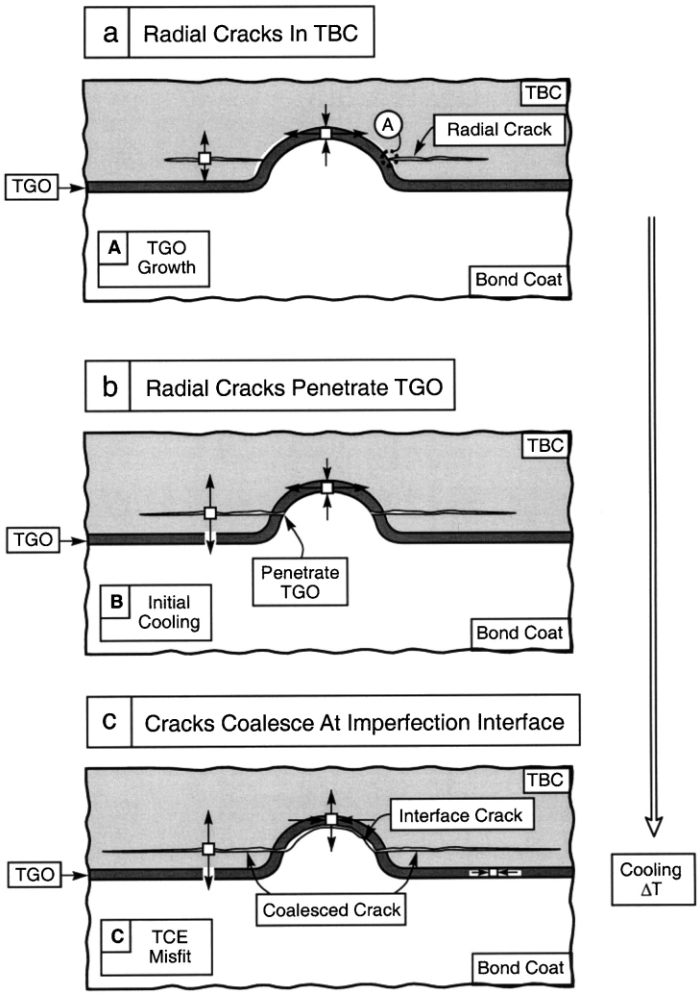

Fig. 25. Cracking sequence caused by growth misfit, followed by cooling to ambient. The radial crack in the TBC penetrates the TGO at its inner edge upon thermal cycling, because of the large stress intensity factor. Thereafter it coalesces along the interface [41,44].

$$a/R = \left[\frac{3\sigma^* \sqrt{R}}{2(1+\upsilon)\sqrt{\pi} K_{\mathrm{Ic}}^{\mathrm{tbc}}}\right] \tag{13}$$

where

$$\sigma^* = \frac{E(m-1)}{3(1-\nu)m}\left(\frac{h}{R}\right)$$

This result implies that the delaminations form preferentially at the larger imperfections. They are also larger for TBCs having low toughness. Note that, while the ultimate extent of these cracks is governed by growth strains, thermal expansion misfit (with cycling) is still an essential element. That is, only upon cooling are stresses induced that separate the interface and cause the cracking of the TGO: events that result in the continuous crack configuration represented by Fig. 25c.

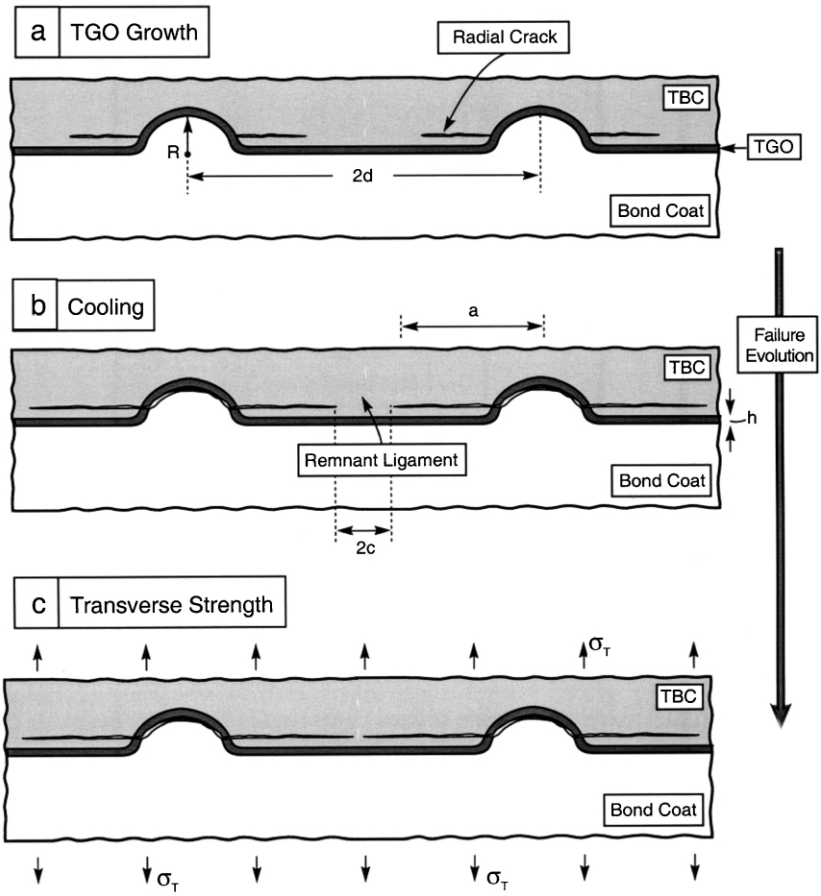

Fig. 26. Schematic of the coalescence of cracks emanating from neighboring imperfections.

Equating the crack diameter in (4) to the spacing between imperfections (Fig. 26) yields a critical TGO thickness, h_c, given by [41]:

$$h_c = \frac{2\sqrt{\pi}(1-\nu^2)md^{3/2}K_{Ic}^{tbc}}{(m-1)RE_{tbc}} \tag{14}$$

Note that the imperfections exert an important influence, through their diameter $2R$, and spacing $2d$. Moreover, since h_c depends on time-at-temperature [in accordance with (1)], then (14) can be re-expressed as a failure time:

$$t_f = h_c^2/2k_p \tag{15}$$

Recall that k_p is a strong function of temperature (Table 2) and that K_{Ic}^{tbc} is sensitive to the TBC microstructure. These later results [(14) and (15)] can be used as the basis for durability models.

Upon extensive thermal cycling combinations of thermal expansion misfit and growth strains in the presence of initial imperfections, cause the TGO to grow into the bond coat by a ratcheting mechanism [37,82] (Appendix E). This happens at interface imperfections that exceed a critical amplitude and penetrate preferentially into bond coat grains having a soft orientation. The consequence is that tensile stresses are induced in the superposed TBC. These are sufficiently large that cracks are readily initiated, causing the response to be governed by the ratcheting displacement, Δ_R. While a full model that relates Δ_R to the misfit strains and the material properties has yet to be devised, some insight can be gained from scaling arguments. If the ratcheting rate, $d\Delta_R/dN$, is specified, the cycles-to-failure has the dependence [Appendix E, (E2)]:

$$N_f \approx 2\sqrt{\pi}(1-\nu^2)d^{3/2}K_{Ic}^{tbc}/E(d\Delta_R/dN)L \tag{16}$$

where $2L$ is the imperfection wavelength. In turn, the ratcheting rate is expected to be roughly proportional to the growth strain, m, and dependent on the bond coat yield strength relative to the thermal expansion misfit stress, as well as the initial imperfection amplitude relative to the critical size.

4. Closure

Aspects of the performance and durability of thermal barrier systems have been clarified through studies of the material state at various fractions of life. All of this effort has been on commercially produced materials with "standard" compositions, microstructures and imperfection "states". This has lead to some understanding of the mechanisms that govern durability. In turn, the mechanistic understanding has been used to develop models of TBC life that contain the controlling material and topological parameters. That is, they reveal the interplay between the key material properties and imperfection topologies, expressed in terms of scaling laws.

As the measurements and observations have become more extensive, seemingly disparate findings all converge into patterns that suggest four simple principles:

i. Compressions in the TGO around interface imperfections, caused by growth and thermal expansion misfit, provide the underlying motivation.

ii. These misfits induce energy release rates at cracks emanating from the major imperfections large enough to exceed the delamination toughness of the TBC.

iii. The coalescence of these cracks results in a separation large enough to satisfy large scale buckling and spalling.

iv. In high cycle scenarios, the combined misfit (from growth and thermal contraction) enlarges the imperfections by a ratcheting mechanism, amplifying the energy release rates and accelerating failure.

The two major deficiencies in the present status concern: (a) the paucity of model validation and (b) as yet, a lack of effort on performance improvements guided by the implications of the models. Both require that materials and imperfections be systematically varied within a parameter space suggested by the models. In turn, this needs a capability for depositing the bond coat and the TBC with control of the surface/interface topology, microstructure and micro-chemistry. Until recently, such approaches and capabilities have not been within the grasp of the research community. Efforts of this type should provide an informed basis for designing superior TBC systems.

Appendix A. Small scale buckling

A1. Buckling maps

The buckling and buckle propagation stages of failure can be succinctly represented by a buckling map. The map is developed upon defining three non-dimensional indices, with three associated domains (Fig. A1). The indices comprise [56,70]:

i. An adhesion index:

$$\Sigma = \sigma_o \sqrt{\frac{(1-\nu)h}{E_0 \Gamma_i^0}} \tag{A1}$$

ii. A buckling index:

$$\Pi = (1-\nu^2)(\sigma_0/E_0)(b/h)^2 \tag{A2}$$

iii. The mode mixity index, λ [Eq. (9)].

The map assumes the pre-existence of an interface separation, size b_0. Modifications to the map that address nucleation are established later. The three domains associated with the buckling map (Fig. A1) are as follows.

- *Domain I.* Stable separations exist because the buckling condition is not satisfied.

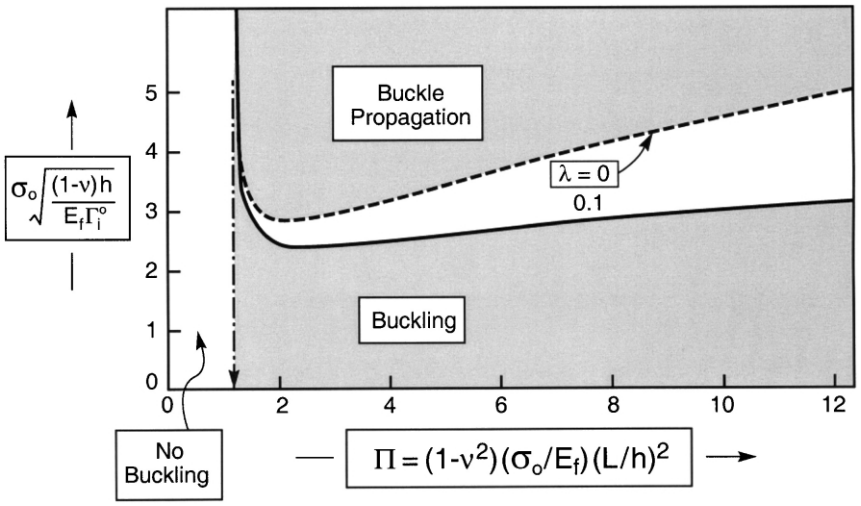

Fig. A1. (Small scale) buckling map relevant to the TGO, showing the buckle propagation domain (top right).

- *Domain II*. The buckling condition is satisfied, but the energy release rate is too low to cause propagation. The transition between I/II occurs at a critical buckling index, $\Pi_c \approx 1.22$. Accordingly, buckling happens at a TGO thickness, h_b, given by:

$$h_b = b_0[(1-\nu^2)\sigma_0/\Pi_c E_0]^{1/2} \tag{A3}$$

  For typical stresses ($\sigma_0 \approx 3$ GPa, Table 1), the critical buckling radius has magnitude: $b_0/h_b \approx 11$.

- *Domain III*. The energy release rate exceeds the interface fracture energy. The transition occurs when the adhesion index is in the range $\Sigma \approx 2-3$, dependent on Π and λ. Buckles propagate when Σ and Π reside along the region II/III transition line, at the relevant λ. At fixed λ, the buckle enlarges stably: that is, Π increases as Σ increases. This happens when either σ_0 or h increase and/or Γ_i^0 decreases upon segregation, fatigue, etc. The stability is enabled by the mode mixity effect on interface toughness, manifest in λ.

Superposing trajectories onto the map specifies conditions wherein the TGO buckles, as well as when the buckle abruptly propagates and arrests. One illustration is given in Fig. A2. It represents a simple thermo-mechanical loading. Following TGO growth at high temperature, to thickness h_0, cooling to ambient establishes a residual compression, σ_0. Then, present an interface separation, radius b_0, induced around a TGO defect, (A2) and (A3) give initial values of the coordinates Σ and Π,

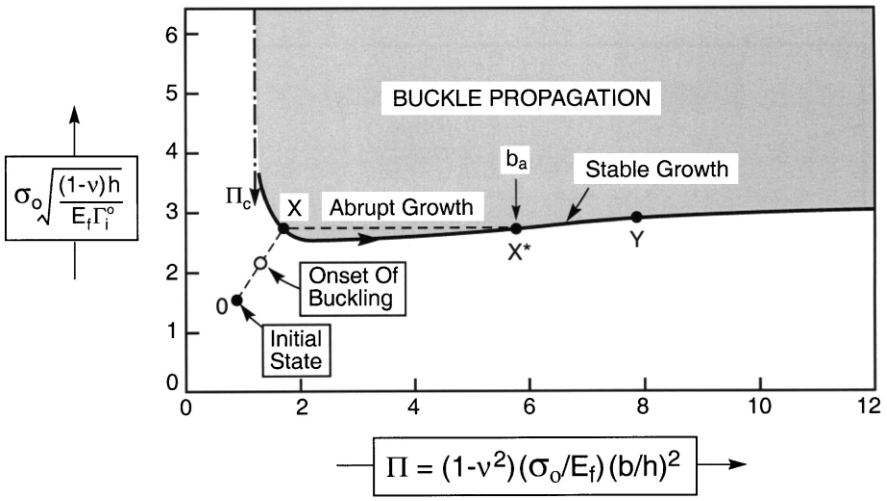

Fig. A2. Prototypical trajectory superposed on the buckling map due to cooling showing the onset of buckling, the initiation of buckle growth (at X) and buckle arrest (at X^*), followed by stable growth along X^*Y as the strain is further increased.

located at position O on Fig. A2. In this example, segregation levels are fixed such that Γ^0 is constant. Subsequent mechanical loading (say, because of bending) causes the compression in the TGO to increase. This stress elevation increases both Σ and Π proportionally [see (A2) and (A3)], resulting in a diagonal trajectory on the buckling map. When the stress elevation causes the trajectory to intersect the buckling transition at O', the TGO buckles, but remains stable if there are no further changes in stress. Additional stress elevation causes the trajectory to reach X. Now, at constant Σ (fixed stress) there will be an abrupt increase in buckle size, as Π jumps over to the region II/III transition, at X^*. Here the buckle arrests at radius, b_a, much enlarged relative to b_0. However, it remains stable at this size until either the stress increases again or Γ_i^0 decreases. Subsequent elevations in stress would cause the buckle to expand stably along X^*Y until either cracking or spalling conditions are satisfied. Because of the shallow trajectory of the region II/III transition, quite small changes in stress enable the final phase to proceed to completion.

A2. Role of imperfections

The influence of imperfections is illustrated by a trajectory superposed on a revised buckling map [70,72] (Fig. A3). Present an initial interface defect, as Σ increases, a critical level is reached (position A) at which a separation pops-in to a stable size, b_i (position B). When Σ further increases, the separation expands stably up to the maximum (point C). Here the separation buckles and abruptly expands to b_0 (point D). At this stage, the buckle may either spall or arrest, depending on conditions relative to the spall criterion. If it arrests, it can again expand stably as Σ increases, until spalling conditions are reached.

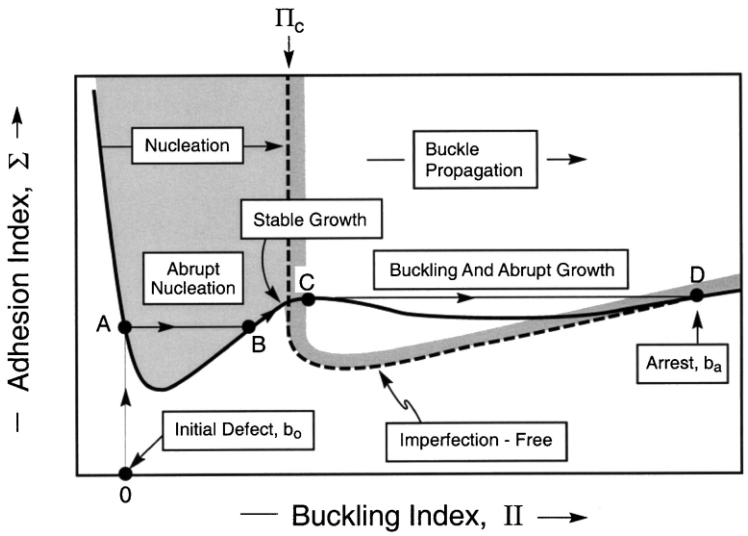

Fig. A3. The influence of imperfections in the TGO on the initiation of the buckling process [72].

Appendix B. Stresses

Preliminary results for the stresses in the TBC, TGO and bond coat are estimated by considering imperfections having spherical symmetry [41,79,80] (Fig. B1). While there are obvious limitations of this geometry, numerical results for more relevant configurations have revealed [41] that the stresses near the apex of the undulation are reasonably well ordered in sign and magnitude.

B1. Thermal expansion misfit

The elastic solutions for thermal expansion misfit in a tri-material system with spherical symmetry have been derived using the "Eshelby" protocol [41,80] (see Fig. 17). The case of interest is one wherein the TGO has the lowest thermal expansion coefficient, α_0, the substrate the largest, α_s, and the TBC the intermediate, α_{tbc}. The stresses in the substrate/bond coat are:

$$\sigma_{rr} = \sigma_{\theta\theta} = \Lambda(\alpha_{tbc} - \alpha_s) \tag{B1a}$$

where ΔT is the cooling range (negative in sign) and $\Lambda = 4\kappa\mu\Delta T[\kappa + 4\mu/3]$, $\mu = E[2(1+\nu)]$, $\kappa = E/[3(1-2\nu)]$. Accordingly, the bond coat is in a state of hydrostatic tension, independent of α_0. The stresses in the TGO are:

$$\sigma_{rr} = \Lambda\{\alpha_{tbc} - \alpha_0 - (\alpha_s - \alpha_0)[(R-h)/r]^3\}$$
$$\sigma_{\theta\theta} = \Lambda\{\alpha_{tbc} - \alpha_0 + \frac{1}{2}(\alpha_s - \alpha_0)[(R-h)/r]^3\} \tag{B1b}$$

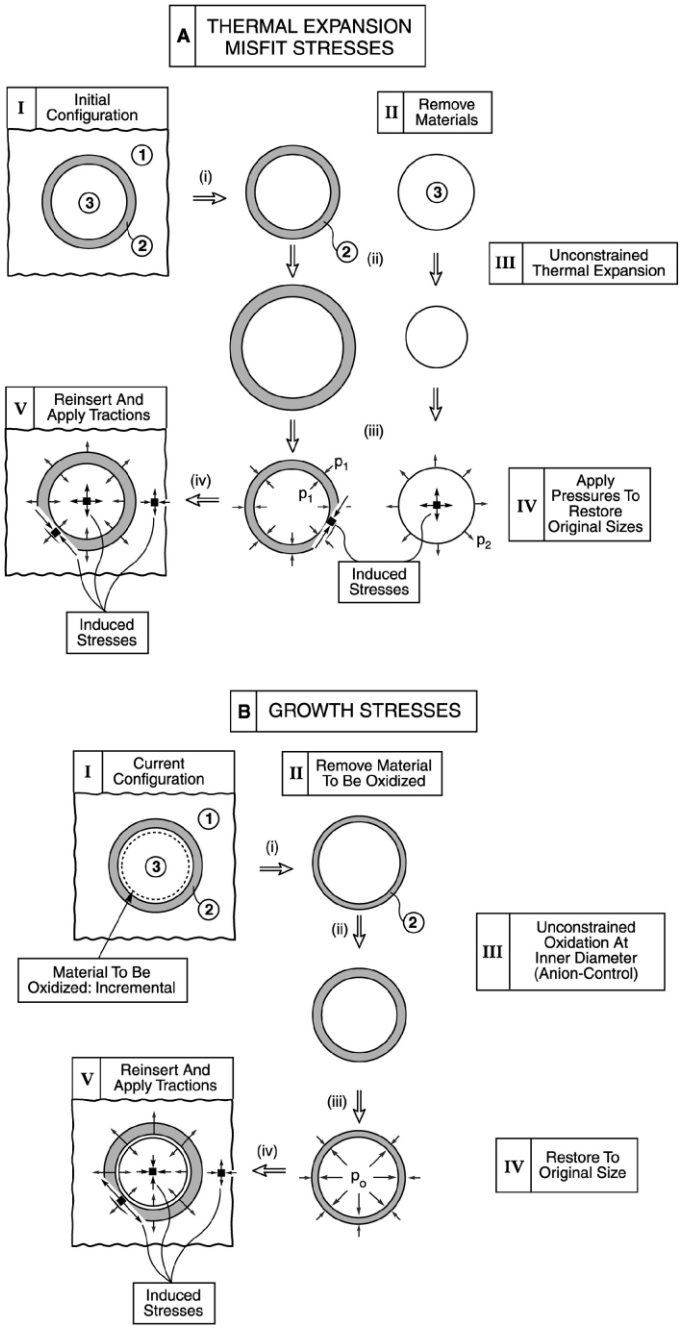

Fig. B1. The stresses that develop around spherical imperfections illustrated by using the ''Eshelby'' procedure. (A) Thermal expansion misfit, (B) anion-controlled TGO growth. The three regions are as follows: (1) the TBC, (2) the TGO and (3) the bond coat/substrate combinations.

where $2R$ is the diameter of the imperfection. Note that since, $\alpha_s > \alpha_{tbc} > \alpha_0$, the TGO is always in hoop compression and the interface between the substrate and the TGO is in radial tension. The stresses in the TBC are:

$$\sigma_{rr} = -2\sigma_{\theta\theta} = -\Lambda\{\alpha_0 - \alpha_{tbc} + (\alpha_s - \alpha_0)(1 - h/R)^3\}(R/r)^3 \tag{B1c}$$

In this case, the sign of the stresses depend on the relative TGO thickness, h/R. When the TGO is thin, the second term in the parentheses dominates and the TBC is in radial compression. Above a critical TGO thickness, radial tension develops. This thickness, h_*, is given by:

$$h_*/R = 1 - [(\alpha_{tbc} - \alpha_0)/(\alpha_s - \alpha_0)]^{1/3} \tag{B2}$$

B2. Oxide growth

The stresses induced by TGO growth differ because the misfit strain occurs predominately at one of the interfaces [41]. For anion-control, governed by inward diffusion of oxygen, the misfit occurs at the interface where the bond coat is consumed. For cation-control, the new oxide forms at the TGO/TBC interface, through the outward diffusion of Al (as well as Ni, Cr, etc.). To determine the stresses, the ratio of new TGO volume to consumed bond coat volume is taken to be m. For anion-control, the stresses within the bond coat are [41],

$$\sigma_{rr} = \sigma_{\theta\theta} = -\frac{2E(m-1)}{3(1-\nu)m}\left(\frac{h}{R}\right) \tag{B3a}$$

In the TBC, $r \geqslant R$,

$$\sigma_{rr} = -2\sigma_{\theta\theta} = -\frac{2E(m-1)}{3(1-\nu)m}\left(\frac{h}{R}\right)\left(\frac{R}{r}\right)^3 \tag{B3b}$$

and within the TGO, $R - h \leqslant r \leqslant R$,

$$\sigma_{rr} = -\frac{2E(m-1)}{3(1-\nu)m}\frac{h}{R}$$
$$\sigma_{\theta\theta} = \sigma^i_{\theta\theta} + \frac{E(m-1)}{3(1-\nu)m}\left[\frac{r}{R} - \left(1 - \frac{h}{R}\right)\right] \tag{B3c}$$

These results have the following features. The TBC is in radial compression and hoop tension. In the TGO, the radial stress is compressive, while the hoop stress is $\sigma^i_{\theta\theta}$ at the growth interface and $\sigma^i_{\theta\theta} + E(m-1)h/[3(1-\nu)mR]$ at the TGO/TBC interface.

For cation-control, the stresses in the bond coat and in the TBC as well as the radial stress in the TGO remain the same. The only difference is in the hoop stress within the TGO ($R - h < r < R$):

$$\sigma_{\theta\theta} = \sigma^i_{\theta\theta} - \frac{9E}{4(1-\nu)}\left(1 - \frac{r}{R}\right) \tag{B4}$$

Appendix C. Stress intensity factors

Radial cracks, radius, a, that form in the TBC as a consequence of the growth misfit have stress intensity factors, K, at the inner and outer crack edges given by [41,81]:

$$\frac{K}{\sigma^*\sqrt{R}} = \sqrt{\frac{\pi}{2}\left(\frac{a}{R} - 1\right)}\left(\frac{R}{a}\right)^{2.4} \text{(outer crack edge)} \tag{C1a}$$

$$\frac{K}{\sigma^*\sqrt{R}} = \sqrt{\frac{\pi}{2}\left(\frac{a}{R} - 1\right)}\left(\frac{R}{a}\right)^{0.55} \text{(inner crack edge)} \tag{C1b}$$

where

$$\sigma^* = \frac{E(m-1)}{3(1-\nu)m}\left(\frac{h}{R}\right)$$

These results are plotted in Fig. C1. Note the very large stress intensity at the inner front. It is this intensity that motivates the crack to penetrate the TGO and coalesce along the interface as the system thermally cycles. When this happens, the resulting stress intensity factor for the larger a/R of interest is [41]:

$$\frac{K}{\sigma^*\sqrt{R}} = \frac{3}{2(1+\nu)\sqrt{\pi}}\left(\frac{R}{a}\right)^{3/2} \tag{C2}$$

This is the result used in the text to predict cracking and failure.

Appendix D. TGO creep/growth dynamics

When a small fraction, β, of the newly formed TGO is manifest as a spatially uniform addition of matter to the vertical grain boundaries in the TGO (see Fig. 16), the in-plane displacement-rate $\dot{\delta}$ on a planar section is:

$$\dot{\delta} = \beta \dot{h} g/h. \tag{D1}$$

such that the in-plane extension-rate is:

$$\dot{\varepsilon}^g_{xx} \equiv \dot{\delta}/g = \beta \dot{h}/h \tag{D2}$$

With (1), the strain-rate becomes:

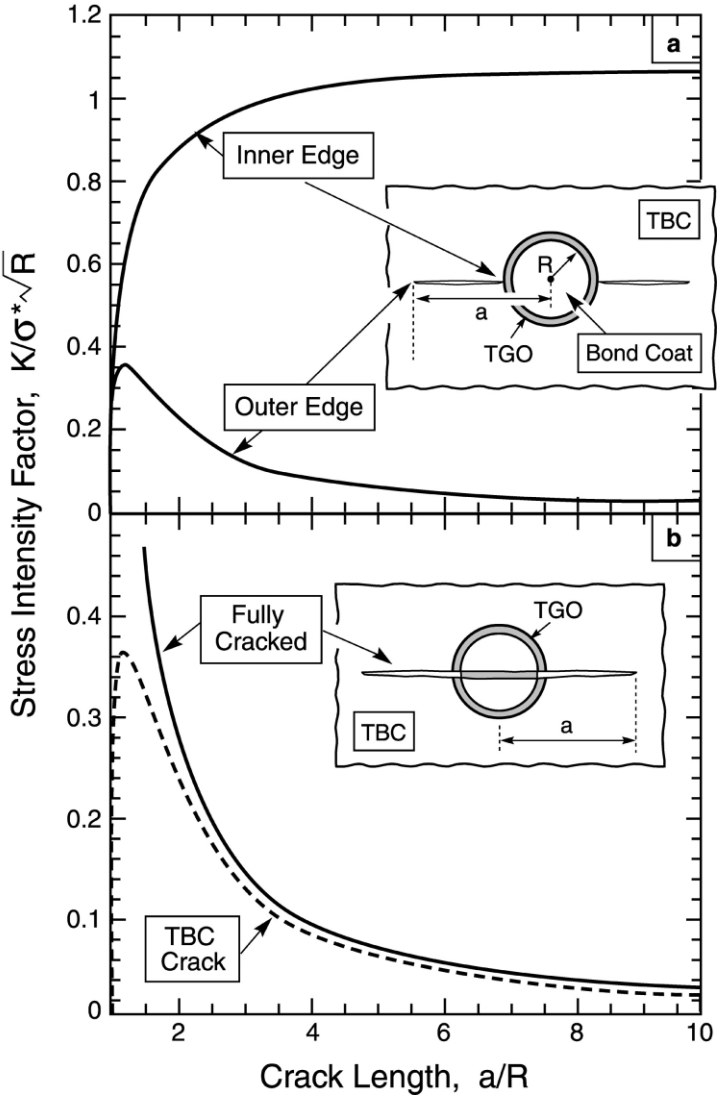

Fig. C1. Stress intensity factors calculated for the crack configurations depicted in the insets.

$$\dot{\varepsilon}^{g}_{xx} = 2\beta k_p / h^2 \tag{D3}$$

Upon equating the strain-rate in (D3) with that in (8), for growth/creep equilibrium (zero net strain-rate), the growth stress for an equi-axed TGO becomes:

$$\frac{\sigma_0}{\mu_0} = -\left(\frac{g}{h}\right)\sqrt{2\beta\,\Sigma}_* \tag{D4}$$

where

$$\Sigma_* = k_p/\dot{\varepsilon}_* \Omega_{Al_2O_3}^{2/3}$$

$$\dot{\varepsilon}_* = 100\left[\frac{D_b \delta_b \mu}{kT}\right]$$

Temperature and compositional effects are manifest in the non-dimensional kinetic ratio: Σ_* (Table 2). The tendency for σ_0 to decrease with increase in TGO thickness (D4) would be mediated by increases in grain size and would become invariant whenever $h \approx g$.

Appendix E. Ratcheting

Thin films on ductile substrates when residually compressed by a misfit stress are susceptible to various out-of-plane displacement instabilities. These displacements occur by distorting the substrate. Pre-existing undulations initiate the instability. Under some circumstances, the undulations increase in amplitude, with thermal cycling, by "ratcheting" [37]. When this happens, the increase in undulation amplitude induces out-of-plane tensile strains in the TBC. These strains cause cracks parallel to the interface which, in turn, induce failures.

Steady-state ratcheting arises when the growth and thermal expansion misfit combine in such a manner that the growth biases the strain by diminishing reverse yielding of the bond coat. That is, absent growth, cyclic yielding occurs as the TGO displaces around an average location established after the first few cycles: whereas, a growth strain causes the TGO to grow into the bond coat with each thermal cycle. The observations [82] and analyses [37] of this phenomenon suggest that two factors dictate the sites at which the ratcheting occurs. (i) Initial interface imperfections above a critical amplitude are needed to induce stresses in excess of the cyclic yield strength of the bond coat. (ii) Because of the extreme yield strength anisotropy of β-NiAl, some grains adjacent to the TGO exhibit a soft orientation in the sense that they are highly susceptible to plastic straining normal to the interface. This combination of orientation softness with interfacial imperfections dictates the ratcheting locations and, thereby, governs the TBC durability.

When undulations in the TGO ratchet in a steady-state manner with rate, $d\Delta_R/dN$, the stress intensity factor at a crack, radius a, in the TBC just above the interface with the TGO can be estimated as:

$$K \approx \frac{E(d\Delta_R/dN)}{2\sqrt{\pi}(1-\nu^2)\sqrt{L}}\left(\frac{L}{a}\right)^{3/2} N \tag{E1}$$

where $2L$ is the wavelength and N the number of thermal cycles. This formula is approximate since the elastic modulus mismatch is not taken into account.

Accordingly, with $2d$ as the spacing between neighboring undulations, the cycles to failure would be:

$$N_f \approx 2\sqrt{\pi}(1-\nu^2)d^{3/2}K_{Ic}^{tbc}/E(d\Delta_R/dN)L \quad \text{(E2)}$$

It remains to relate the ratcheting rate to the misfit strains and the physical properties of the system.

References

[1] Miller RA. J Amer Ceram Soc 1984;67:517.
[2] Mariochocchi A, Bartz A, Wortman D. Thermal barrier coating workshop. NASA CP 3312, 1995. p. 79.
[3] Bose S, DeMasi-Marcin J. Thermal barrier coating workshop. NASA CP 3312, 1995. p. 63.
[4] DeMasi-Marcin JT, Gupta DK. Surf Coatings Tech 1994;68/69:1–9.
[5] Hillery R, editor. NRC report. Coatings for high temperature structural materials. National Academy Press, 1996.
[6] Strangman TE. Thin Solid Films 1985;127:93–105.
[7] Meier SM, Gupta DK. Trans ASME 1993;116:250–7.
[8] Wright PK, Evans AG. Current Opinion in Solid State and Materials Science 1999;4:255–65.
[9] Wright PK. Mat Sci Eng 1998;A245:191–200.
[10] Cruse TA, Stewart SE, Ortiz M. J Eng Gas Turbines Power 1988;110:610.
[11] Bennett A, Toriz F, Thakker A. Surface and Coating Technology 1987;32:227–36.
[12] Meier SM, Nissley DM, Sheffler KD. Thermal barrier coating life prediction model development — phase II. NASA CR-18911, July 1991.
[13] Kingery WD, Bowen HK, Uhlmann DR. Introduction to ceramics. New York: Wiley and Sons, 1976
[14] Rigney DV, Viguie R, Wortman DJ, Skelly WW. Proc of the Workshop on Thermal Barrier Coatings, NASA-CP-3312. NASA Lewis Research Center, 1995. p. 135–50.
[15] DeMasi-Marcin JT, Sheffler KD, Bose S. ASME Paper 89-GT-132. New York: American Society of Mechanical Engineering, 1989.
[16] Lee EY, Sisson RD. In: Berndt CC, Sampath S. editors. Proc 7th National Thermal Spray Conference, Boston, MA, 20–24 June. Materials Park, OH: ASM International, 1994. p. 55–9.
[17] Choi SR, Zhu D, Miller RA. Ceramic Engineering and Science 1998;19:293–301.
[18] Golightly FA, Stott FH, Wood GC. Oxid Metals 1976;10:163.
[19] Stiger MJ, Yanar NM, Topping MG, Pettit FS, Meier GH. Z. Metallk 1999;90:1069–78.
[20] Quadakkers WJ, Tyagi AK, Clemens D, Anton R, Singheiser L. In: Hampikian JM, Dahotre NB, editors. Elevated temperature coatings: science and technology, Warrendale (PA): TMS, 1999. p. 119.
[21] Lipkin DM, Clarke DR. Oxid Metals 1996;45:267–80.
[22] Tolpygo VK, Clarke DR. Oxid Metals 1998;49:187–211.
[23] Mennicke C, Schumann E, Ulrich C, Ruehle M. Mater Sci Forum 1997;389:251–4.
[24] Sergo V, Clarke DR. J Amer Ceram Soc 1998;81:3237–42.
[25] Tolpygo VK, Clarke DR. Acta Mater 1998;46:5153–66.
[26] Christensen RJ, Tolpygo VK, Clarke DR. Acta Mater 1997;45:1761–6.
[27] Sarioglu C, Blachere JR, Pettit FS, Meier GH. In: Newcomb SB, Little JA, editors. London: Microscopy of oxidation 3. The Institute of Materials, 1997. p. 41.
[28] Smeggil JG. Mater Sci Engr 1987;87:261–5.
[29] Smialek JL, Jayne DT, Schaeffer JC, Murphy WH. Thin Solid Films 1994;253:285–92.
[30] Meier GH, Pettit FS. Report on AFOSR Contract F49620-981-0221. Univ. of Pittsburgh, 1 September, 1999.
[31] Haynes JA, Zhang Y, Lee WY, Pint BA, Wright IG, Cooley KM. In: Hampiklan JM, Dahotre NB,

editors. Elevated temperature coatings: science and technology. Warrendale (PA): TMS; 1999. p. 185.
[32] Schaeffer J, Kim GM, Meier GH, Pettit FS. In: Lang E, editors. The role of active elements in the oxidation behavior of high temperature metals and alloys. Elsevier, 1989. p. 231.
[33] Nicholls JR. Materials Science Forum 1997;935:251–4.
[34] He MY, Evans AG, Hutchinson JW. Mat Sci Eng 1998;A245:168–81.
[35] Gong X-Y, Clarke DR. Oxidation of Metals 1998;50(3/4):355–76.
[36] Gell M, Vaidyanathan K, Barber B, Cheng J, Jordan E. Met Mater Trans 1999;30A:427.
[37] He MY, Evans AG, Hutchinson JW. Acta Mater 2000;48:2593–601.
[38] Evans AG, Hutchinson JW, He MY. Acta Mater 1999;47:1513–22.
[39] Suresh S. Fatigue of materials. 2nd ed. Cambridge University Press, 1998.
[40] Choi SR, Hutchinson JW, Evans AG. Mechanics Materials 1999;31:431–47.
[41] Evans AG, He MY, Hutchinson JW. Progress in Materials Science 2001;46:249–71.
[42] Mumm DR, Evans AG. Acta Mater 2000;48:1815–27.
[43] Evans AG, Hutchinson JW, Wei YG. Acta Mater 1999;47:4093–113.
[44] Rabiei A, Evans, AG. Acta Mater 2000;48:3963–76.
[45] Clarke DR, Sergo V, He MY. In: Hampikian JM, Dahotre NB, editors. Elevated temperature coatings: science and technology. Warrendale (PA): TMS, 1999. p. 67.
[46] Mennicke C, Mumm DR, Clarke DR. Z Metallk 1999;90:1079–85.
[47] Graham MJ, Eldridge JI, Mitchell DF, Hussey RJ. Mater Sci For 1989;43:207.
[48] Ruehle M. Unpublished research.
[49] Steiner A, Komarek KL. TMS-AIME 1964;230:786–90.
[50] Rhines FN, Wolf JS. Met Trans 1970;1:1701–10.
[51] Dove DB, Baldwin DH. Met Trans 1974;5:1637–41.
[52] Cannon RM, Rhodes WH, Heuer AH. J Am Ceram Soc 1980;63:46.
[53] Cho J, Harmer MP, Chan HM, Rickman JM, Thompson AM. J Am Ceram Soc 1997;80:1013.
[54] Fang J, Thompson AM, Harmer MP, Chan HM. J Am Ceram Soc 1997;80:2005.
[55] Schumann E, Sarioglu C, Blachere JR, Pettit FS, Meier GH. Oxid Metals 2000;53:259.
[56] Hutchinson JW, Suo Z. Adv Appl Mech 1992;29:62–191.
[57] Bree J. J Strain Analysis 1968;3:122–7.
[58] Jansson S, Leckie FA. J Mech Phys Solids 1992;40:593–612.
[59] Cannon RM, Hou PY. In: McNallan M et al., editors. High temperature corrosion and materials chemistry. Electrochemistry Society Proc 1998;98/99:594.
[60] Evans AG, Cannon RM. Mater Sci Forum 1989;43:243.
[61] Hindam H, Whittle DP. Oxid Met 1982;18:245.
[62] Brumm MW, Grabke HJ. Corros Sci 1992;33:1677.
[63] Stott FH, Atkinson A. Materials at High Temperatures 1994;12:195.
[64] Huntz AM, Schutze M. Materials at High Temperatures 1994;12:151.
[65] Frost HJ, Ashby MF. Deformation mechanism maps. New York: Pergamon Press, 1982.
[66] Gaudette FA, Suresh S, Evans AG, Dehm G, Ruhle M. Acta Mater 1997;45:3503–14.
[67] Lipkin D, Clarke DR, Evans AG. Acta Mater 1998;46:4835–50.
[68] Gaudette FA, Suresh S, Evans AG. Met Mater Trans 2000;31A:1977–83.
[69] Janakiraman R, Meier GH, Pettit FS. Metall and Mater Trans A 1999;30A:2905.
[70] Wang JS, Evans AG. Acta mater 1999;47:699–710.
[71] Wang JS, Sugimura Y, Evans AG, Tredway WK. Thin Solid Films 1998;325:163–74.
[72] Hutchinson JW, He MY, Evans AG. Journal of Mech and Phys of Solids 2000;48:709–34.
[73] Levi CG, Yang JY, Dalgleish BJ, Zok FW, Evans AG. J Am Ceram Soc 1998;81:2077–86.
[74] Johnson CA, Ruud JA, Bruce R, Wortman D. Surf Coatings Tech 1998;108/109:80.
[75] Clyne TW, Gill SC. J Thermal Spray Tech 1996;5:401–18.
[76] Bartlett AH, DeMaschio R. J Am Ceram Soc 1995;78:1018–24.
[77] Tsui YC, Clyne TW. In: Berndt CC, editor. Thermal spray: practical solutions for engineering problems. ASM International, 1996. p. 275.
[78] McPherson R. Thin Solid Films 1981;83:297.

[79] Balint DS, Hutchinson JW. Unpublished research.
[80] Hsueh CH, Fuller ER Jr. Mat Sci and Engr 2000;A283:46–55.
[81] Shum DKM, Huang YY. Engr Fract Mech 1990;37:107–17.
[82] Mumm DR, Evans AG, Spitsberg IT. Acta Mater, in press.
[83] Nicholls JB, Lawson KJ, Rickerby DS, Morell P, AGARD REPORT R-823, April 1998.